

5-2019

# Characterization of Trap Frequencies for Cold Atom Laboratory Bose-Einstein Condensates

Maxwell Jeremy Gold  
mgold@bates.edu

Follow this and additional works at: <https://scarab.bates.edu/honorstheses>

---

## Recommended Citation

Gold, Maxwell Jeremy, "Characterization of Trap Frequencies for Cold Atom Laboratory Bose-Einstein Condensates" (2019). *Honors Theses*. 288.  
<https://scarab.bates.edu/honorstheses/288>

This Restricted: Embargoed [Open Access After Expiration] is brought to you for free and open access by the Capstone Projects at SCARAB. It has been accepted for inclusion in Honors Theses by an authorized administrator of SCARAB. For more information, please contact [batesscarab@bates.edu](mailto:batesscarab@bates.edu).

# Characterization of Trap Frequencies for Cold Atom Laboratory Bose-Einstein Condensates

Maxwell Jeremy Gold

Advised by Professor Nathan Lundblad

## An Honors Thesis

Presented to the Department of Physics and Astronomy

Bates College

in Partial Fulfillment of the requirements for the

Degree of Bachelor of Arts

Lewiston, Maine

March 2019



## Abstract

With the recent production of Bose-Einstein condensates using NASA's Cold Atom Laboratory (CAL) aboard the International Space Station, research is underway focusing on the extent to which quantum mechanics can be studied in a microgravity environment. These condensates have the potential to be the coldest ever studied in experiment and in free-fall their place in orbit allows us to observe them in long time-of-flights. This thesis reports fitting analyses and trap frequency characterization of imaging data from condensates in conventional magnetic potentials. This information will be used for the calibration and design of future experiments with CAL, regarding both conventional and radio-frequency dressed traps. Of particular interest to further study are ellipsoidal shell condensates and the quasi-two-dimensional condensate that exists on its surface in the limit of low shell thickness.



## Acknowledgements

I would like to express my deep thanks to Nathan Lundblad for advising me on this project. In the two years I have been your student I have learned of an entire world of physics and gotten to play with its technology. Your patience with me has been a pillar of my belonging to this school. To my parents I am forever grateful for the opportunities you have afforded me in this education. And for all my things. To my friends, my roommates, and all the others that exist within my sphere, thank you for the energy you have provided me in this environment. Lastly a special thanks to Ceri Kurtz, who has been there for me in these last two years, and for whom I wish a speedy recovery.



# Contents

<b>Abstract</b>	<b>i</b>
<b>Acknowledgements</b>	<b>iii</b>
<b>1 Introduction</b>	<b>1</b>
<b>2 Theory</b>	<b>4</b>
2.1 Bose-Einstein Statistics and Condensation . . . . .	4
2.2 The Thomas-Fermi Approximation . . . . .	10
2.3 Rubidium-87 . . . . .	13
2.4 The Trapping and Cooling of Atoms . . . . .	16
2.5 Bose-Einstein Condensate Dynamics . . . . .	23
<b>3 Apparatus</b>	<b>26</b>
3.1 The CAL Science Chamber . . . . .	27
3.2 The Atom Chip . . . . .	28
3.3 Radio-Frequency Dressing . . . . .	31
3.4 Imaging . . . . .	33



<b>4</b>	<b>Analysis</b>	<b>36</b>
4.1	Overview of Code . . . . .	37
4.2	Fitting Center, Number, and Temperature . . . . .	38
4.3	UFOs (Unidentified Free-falling Objects) . . . . .	45
4.4	Trap Frequency Characterization via Non-Adiabatic Ramp . . . . .	46
4.5	Adiabatic Ramp and Mysterious Heating . . . . .	48
<b>5</b>	<b>Looking Forward</b>	<b>50</b>
5.1	Mysterious Heating . . . . .	50
5.2	Returning the to Fits . . . . .	51
	<b>References</b>	<b>53</b>

# Chapter 1

## Introduction

A current branch in the study of Bose-Einstein condensates (BEC) is the exploration of trapping potentials in novel topologies and the quasi-lower-dimensional condensates that can be produced within them[1, 2]. Of interest to the research surrounding this thesis is the study of a hollow, “bubble” condensate induced by adiabatic radio-frequency dressing[3, 4, 5]. Current theoretical work on these potentials considers the existence of a super-fluid phase present in the quasi-2D condensate that exists on the surface of this hollow shell in the limit of low shell thickness[5, 6, 7]. Experimentally, however, the presence of a gravitational potential when at rest on the surface of the earth creates a sagging effect in these experiments, disallowing us from studying any of this physics terrestrially in forms other than quasi-2D condensate disks[8, 2]. To combat this in recent years atomic physics has taken to experimentation in microgravity as a means of avoiding this sag. The earliest work surrounding the production of condensates in microgravity sought out a temporarily free-falling frame by releasing an apparatus from a drop tower and taking data within the 9.3 seconds of microgravity made available by this experiment[9, 10, 11]. Subsequent approaches have reached upwards of 6 minutes of microgravity in sounding rockets, performing interferometry and frequency comb experiments on the atoms in that time[12, 13].

This thesis presents results from experiments aboard NASA’s Cold Atom Laboratory (CAL), an apparatus housed within the International Space Station (ISS), in perpetual free-

fall. The novelty of having an arbitrarily long timescale with which we can perform experiments in microgravity, allows us to produce trapping potentials that are among the weakest (i.e. the potential for the coldest condensates) ever explored[14, 15].

I report data from the earliest set of experiments operated with CAL after its installation on the ISS. This work seeks predominately to confirm the behavior predicted by our lab's model of the potentials produced by CAL's atom chip trap[16]. As we confine these atoms to a harmonic well in experiment, I look to characterize the frequencies at which our condensates slosh within their external potentials, given some perturbation to make them do so. In order to analyze this data, I present a set of custom curve fitting routines with which we can map the center-of-mass of motion of our condensates. Additionally I discuss how we can connect these fits to further physical parameters of the atomic cloud, and report estimations for number and temperature of the condensates within this data. Lastly in looking at more recent data taken with CAL, I present some of the ongoing disconnect between our theory and the observations we make in adiabatically ramping an atomic cloud into its final trapping configuration. I demonstrate how my code can be used to quantify the existence of this random heating effect that we currently experience.

In order to enter into this discussion my thesis begins by defining the state of the Bose-Einstein condensate, and the relevant theory to their production in Chapter 2. The barrier of entry to this topic can in fact be reduced to as little quantum mechanics as an understanding of two core concepts: 1.) that all particles have wavelike behavior described by their de Broglie wavelength and the Schrödinger equation for the system the particle occupies, and 2.) that bosons are the class of particles capable of having a large number occupy the same quantum state in a single system. Higher order concepts from this realm of physics are explored, however they pertain mostly to the process of making BECs. Other than an intuition for what these concepts are, the reader only need have an understanding of classical and semi-classical statistical mechanics and thermodynamics (to which I reference [17] for further discussion). There are plenty of didactic texts that take deeper forays into the field of atomic physics and the production of BECs than I have the space to present here[18, 19, 20]. For this reason the definitions and equations I invoke exist for the purposes of bringing a conceptual understanding

---

of what these quantum objects are to light. Thereafter I consider some of the unique specificity of the CAL apparatus in Chapter 3, before launching into my analysis in Chapter 4.

While this thesis unfortunately cannot present the production of this hollow geometry within our BECs, it is significant that the results of this analysis will be employed in the calibration of future bubble trap experiments. An exact understanding of the size, shape, and location of our condensate's conventional confining potential is necessary to deduce how we can overlay the geometry of this additional adiabatic potential on to our condensates. The analysis presented here highlights the connecting bridge between our ability to affirm what we can observe and those future endeavors.

# Chapter 2

## Theory

A boson can be defined explicitly as a particle with an integer spin -  $s = n, n \in \mathbb{Z}$ . Conversely a particle with half-integer spin -  $s = n + \frac{1}{2}, n \in \mathbb{Z}$ , can be defined as a *fermion*. Understanding these definitions beyond where we see their implications empirically requires a relativistic treatment of quantum mechanics[21]. That is outside the domain of this thesis. Instead I will use the first part of this chapter to discuss the statistical governance of boson's behavior *en masse*, in order to set up the condition for Bose-Einstein condensation. We need only a definition of the Pauli exclusion principle to further proceed: that in the case of bosons we can have any number of particles occupying the same state.

Later in this chapter I will discuss the relevant features of  $^{87}\text{Rb}$  and talk about why we choose this species of atom. Finally I will cover the theory of experimentation that is implemented in creating condensates, and address some of the behavior we expect to observe.

### 2.1 Bose-Einstein Statistics and Condensation

In this section I will work towards a definition of Bose-Einstein condensation from a statistical understanding of the behavior of bosons in a collective system. This is by no means a unique derivation and can be found in several textbooks and other theses[18, 17, 4]. Here we do not require an explicit statement about the symmetrization requirement of a boson's

wavefunction in order to reach the conclusion that these particles approach degeneracy at finite low energies[21]. To begin to understand the condition for quantum effects to dominate the statistical behavior of a system, I will briefly refer to a few key results from classical statistical mechanics. The section culminates in the description of a condensate in a harmonic potential. These are the relevant potentials we study in experiment.

Classically we are able to distinguish a particle in a system by its initial position and velocity. The Maxwell-Boltzmann velocity distribution states,

$$f(v) = \left( \frac{m}{2\pi k_B T} \right)^{3/2} e^{-\frac{m|v|^2}{2k_B T}}, \quad (2.1)$$

where  $v$  is magnitude of the particle's velocity,  $k_B$  is Boltzmann's constant,  $m$  is the mass of the particle, and  $T$  is the temperature of the ensemble. This equations tells us that we can determine the probability of a particle having a particular energy from a macroscopically measurable feature of the system like temperature. Here I am referring to the definition of temperature for a classical gas,  $E/N = (f/2)k_B T$ , where the average kinetic energy of a particle is given by the degrees of motion for the particle,  $f$ , scaled by  $\frac{1}{2}k_B T$ .

Evaluating the occupation probabilities of quantum states invokes a few more restraints that force us to redefine our sense of Maxwell-Boltzmann statistics. Instead we look to use what we already know from classical statistical mechanics to describe the behavior of bosons as quanta. Since bosons congregate in the same state infinitely in low energy limits, we can treat each state in the system as a subsystem exchanging particles and energy with the other states. We therefore can treat a given state as a grand canonical ensemble, making the substitutions that  $E_i = N_i \epsilon_i$ . Now consider the subsystem of the ground state with energy,  $E_0 = N_0 \epsilon_0$ . We construct the grand partition function

$$\mathcal{Z} = \sum_i e^{\left[ \frac{-(E_0 - N_i \mu)}{k_B T} \right]} = \sum_i e^{\left[ \frac{-(\epsilon_0 - \mu)}{k_B T} \right]^{N_i}}. \quad (2.2)$$

Since we understand bosons not to obey Pauli exclusion there is no limit to  $N_i$  for this ground state. Equation (2.2) therefore becomes an infinite geometric series converging to

$$\mathcal{Z} = \frac{1}{1 - e^{-(\epsilon_0 - \mu)/k_B T}}. \quad (2.3)$$

A determination of the population distribution can be found from the equation for average particle number:

$$f(\epsilon_0) = \langle N \rangle = k_B T \frac{1}{\mathcal{Z}} \left( \frac{\partial \mathcal{Z}}{\partial \mu} \right)_{V,T} = \frac{1}{e^{(\epsilon_0 - \mu)/k_B T} - 1}. \quad (2.4)$$

We can then write this distribution for any energy level  $\epsilon$  to get the general Bose-Einstein distribution,

$$f_{\text{BE}}(\epsilon) = \frac{1}{e^{(\epsilon - \mu)/k_B T} - 1}. \quad (2.5)$$

This distribution gives us the number of particles we expect to occupy an energy level as a function of temperature and the chemical potential  $\mu$ , describing the change in energy of the system from adding or subtracting atoms of the same species. We can determine a function for the occupation number of  $N_0$  the ground state simply by plugging in the ground state energy  $\epsilon_0$  into this distribution. In rewriting this function we can see the following:

$$\frac{\epsilon_0 - \mu}{k_B T} = \ln \left[ 1 + \frac{1}{N_0} \right] \simeq \frac{1}{N_0}, \quad (2.6)$$

which we can justify when  $N_0$  is sufficiently large, regardless of what fraction  $N_0$  is of the total number. This tells us that the spacing between quantized energies for particles in the system is small compared to an amount of thermal energy at finite temperatures.

Now consider a box of volume,  $\mathcal{V}$ , containing a system of  $N$  atoms. We can write the total number of atoms as the composite of the ground state occupation number and the excited state population as follows,

$$N = N_0 + \int_0^\infty f(\epsilon) D(\epsilon) d\epsilon, \quad D(\epsilon) = \left[ \frac{2\pi(2m)^{3/2}}{h^3} \right] \mathcal{V} \epsilon^{1/2}, \quad (2.7)$$

where  $D$  is the density of states for the confining box. With the Bose-Einstein distribution as it is in Equation (2.5), this integral becomes difficult to solve. However an important result of Equation (2.6), is that we can actually neglect  $\mu$  for all energy levels except the ground state:

$$\epsilon_1 - \mu = (\epsilon_1 - \epsilon_0) + (\epsilon_0 - \mu) \simeq \hbar\omega + \frac{k_B T}{N_0} \simeq \hbar\omega. \quad (2.8)$$

The distribution function for these excited particles under this approximation resembles the distribution for photons given by,

$$f(\epsilon) \simeq \frac{1}{e^{\epsilon/k_B T} - 1} \quad (2.9)$$

This distribution does not conserve number as  $T \rightarrow 0$ , and it allows us to solve the integral in Equation (2.7) analytically by making the substitution  $x = \epsilon/k_B T$ . We find,

$$N = N_0 + \left[ \frac{(2\pi m)^{3/2}}{h^3} \right] V (k_B T)^{3/2} \cdot 2.612 = N_0 + \frac{\mathcal{V}}{\lambda_{\text{TH}}^3} \zeta\left(\frac{3}{2}\right) \quad (2.10)$$

which we can write in terms of the thermal de Broglie wavelength, describing the average wavelength of a particle in the system. Doing so allows us to abstract away from the three dimensional square well we have chosen for a moment and describe the condition for a critical phase-space density more generally. The term notated by  $\zeta$  is a Riemann zeta integral of the form  $\zeta(s) = \frac{1}{\Gamma(s)} \int_0^\infty \frac{x^{s-1}}{e^x - 1} dx$ , where  $\Gamma$  denotes the gamma function. Here,  $\zeta(\frac{3}{2}) = 2.612$ . This is a result of the density of states, and so in a more general case this constant would vary too.

Still it is apparent from this equation that the excited state population is related to an average measure of the delocalized position of particles in the gas, as  $N - N_0 \propto 1/\lambda_{\text{TH}}^3$ . However if we define a critical temperature,  $T_c$ , such that there are no particles in the ground state, we can demonstrate a deeper connection between the probability distribution of these particles and the gas's number density,  $n$ , measuring the concentration of particles in a finite volume. We find,

$$\frac{N}{\mathcal{V}} = n = \frac{\zeta(D(\epsilon))}{(\lambda_{\text{TH}}(T_c))^3}. \quad (2.11)$$

This defines the condition for Bose-Einstein condensation in terms of two parameters: 1.) the critical temperature  $T_c$ , and 2.) a number density (or phase-space density) that is dependant



on our confining volume,  $\mathcal{V}$ . In practice, as we have more capability to create a desired volume, it is more convenient to think  $T_c(\mathcal{V})$  and consider the effect of condensation to be a result of crowding atoms closely together in tight confinement. Equation (2.11) details that this rapid approach towards degeneracy in the ground state occurs when the inner particle spacing is such that individual particles' de Broglie wavelengths begin to overlap. Figure 2.1 depicts this approach as we lower the temperature of our gas. If we want to determine the population of

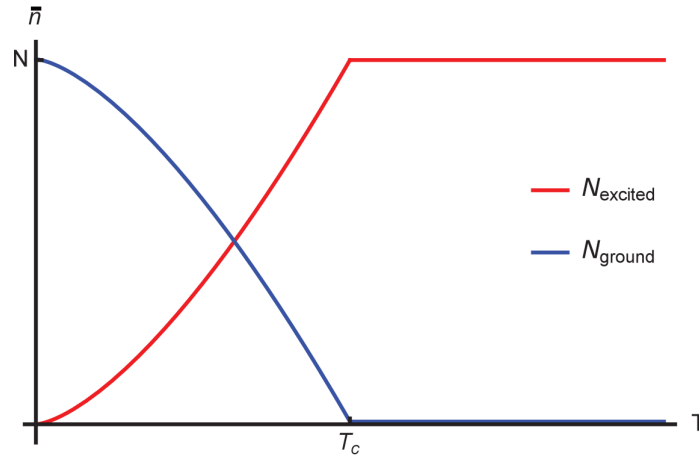


Figure 2.1: Ground state population and excited state population as a function of temperature. [4]

particles that exist in the ground state at finite  $T < T_c$  we have to return again to the hard-wall confinement of the gas's volume that we instated earlier. We can multiply Equation (2.11) by  $\mathcal{V}$  and then divide it from Equation (2.10) to find the following fractional statement,

$$\frac{N_0}{N} = 1 - \left[ \frac{T}{T_c} \right]^{3/2}. \quad (2.12)$$

Note that whatever the value of  $\zeta$ , it has been divided out in this equation.

In thinking about the kinds of harmonic potential wells that we can create in experiment to confine atoms, we can check how this changes the calculations we made above. The root of this variation comes from the integral we solved in Equation (2.10). The density of states for a harmonic potential has  $D(\epsilon) \propto \epsilon^2$ , as opposed to  $\sqrt{\epsilon}$  in the case of a box. This leads to a Riemann zeta function in three dimensional space with a value  $\sim 1.2$  and a relation between the population of the excited states and temperature where  $N - N_0 \propto T^3$  and not  $T^{3/2}$ . Solving

again for the ground state fraction we find,

$$\frac{N_0}{N} = 1 - \left[ \frac{T}{T_c} \right]^3. \quad (2.13)$$

Similarly we can determine the critical temperature we expect for a gas of bosons in this confinement from Equation (2.11). Here we see,

$$T_c = \frac{\hbar \bar{\omega}}{k_B} \left[ \frac{N}{1.202} \right]^{1/3}, \quad (2.14)$$

where  $\bar{\omega} = (\omega_x \omega_y \omega_z)^{1/3}$  is the mean frequency of the harmonic potential[22]. An average tight trap, discussed in Section 3.2, with  $\bar{\omega} = 2\pi \cdot 610$  Hz a cloud of  $N = 140000$  has  $T_c = 1.4$   $\mu$ K[16]. The average weak trap of the same number with  $\bar{\omega} = 2\pi \cdot 67$  Hz has  $T_c = 157$  nK.

The fact that the condensates we produce are made of atomic matter, creates a few more implications for our system. If we focus on an individual atom within the condensate, in the ground state of some potential, we know its energy is described by the solutions to some time-independent Schrödinger equation,

$$\left[ -\frac{\hbar^2}{2m} \nabla^2 + V'(\vec{r}) \right] \psi = \mu \psi. \quad (2.15)$$

Here  $\mu$  is describing the energy of an atom in the presence of others in the system and is equivalent to the chemical potential[18]. I have written the potential energy term with a prime notation to denote that it describes more than the confining potential the collection of atoms experiences. In addition to the trap, atoms experience a potential energy,  $V_0$ , induced by low energy collisions with other atoms in the system. An expression for this term comes from quantum scattering theory, which is aptly discussed in many of this thesis's references[18, 19, 20]. The limit of this theory that is relevant to us is the  $s$ -wave scattering regime, when the energy is low enough such that the relative angular momentum between a pair of atoms is 0. The central result of this limit is a measure of an interaction parameter related to the interaction energy between two atoms, where

$$U_0 = \frac{4\pi \hbar^2 a}{m}. \quad (2.16)$$

The scattering length,  $a$ , is a single parameter characterizing the strength of this interaction. In a very classical understanding of these collision as happening between hard-spheres, this length describes the radius of this sphere representing the atom. In a system of  $N$  atoms, any one atom experiences an interaction potential  $V_0 = N|\psi|^2 \cdot U_0$ , assuming  $N \simeq N - 1$ . If we include this term in our time independent Schrödinger equation we arrive at the Gross-Pitaevskii equation (GPE) which we use to determine the wavefunction of the condensate:

$$\left[ -\frac{\hbar^2}{2M}\nabla^2 + V(\vec{r}) + g|\psi|^2 \right] \psi = \mu\psi, \quad g = \frac{4\pi\hbar^2 Na}{m}, \quad (2.17)$$

In a system where each term on the left side of the GPE plays a significant role in determining the energy, the equation can only be solved numerically. In the next section I will discuss an approximation that allows us to analytically tease out some physical qualities of the condensate.

## 2.2 The Thomas-Fermi Approximation

The previous section contained a description of Bose-Einstein statistics, the definition of the condensate phase, and the building of the Gross-Pitaevskii equation that we use to describe an atom within the condensate. It is reasonable to question then why a particular limit of our understanding of Bose-Einstein condensation gets its own dedicated section. A succinct answer is that the results of this section are those we directly use in analysis of the images of  $^{87}\text{Rb}$  BECs.

At the end of the last section we reached a description of the time-independent Schrödinger equation for a condensate in the form of the GPE,

$$\left[ -\frac{\hbar^2}{2M}\nabla^2 + V(\vec{r}) + g|\psi|^2 \right] \psi = \mu\psi, \quad (2.18)$$

where in the intermediate regime (with kinetic and interaction energy of equal order) this equation yields no analytic solution for  $\psi$ . In the limit where interactions are weak,  $g \sim 0$ , the GPE reduces to a time-independent Schrödinger equation with solutions linked to the external potential the particles experience. This section will focus on the other limit when the

kinetic energy term is negligible, a justification of the large number of atoms and the limit of low temperature that we are in within our experiments. The approximation we make in neglecting the kinetic energy term of the GPE is known as the Thomas-Fermi approximation and leads to a regime in which we can make a number of observations about the condensate phase all within a semi-classical framework. This approximation exists elsewhere in physics rooted in the treatment of quantum mechanics with electron densities rather than wavefunctions[23, 24].

In the limit of the Thomas-Fermi regime we can see that for the region where  $|\psi|^2 \geq 0$  we can rewrite the above equation as

$$|\psi|^2 = \frac{\mu - V(\vec{r})}{g}. \quad (2.19)$$

For the harmonic, external potentials we are studying, where  $V(\vec{r}) = \frac{1}{2}M(\omega_x x^2 + \omega_y y^2 + \omega_z z^2)$ , this approximation leads to a probability density for an atom in the condensate that appears inversely parabolic. Again under the condition that  $|\psi|^2 \geq 0$ , we have:

$$|\psi|^2 = \frac{\mu}{g} \left[ 1 - \frac{M}{2\mu} (\omega_x^2 x^2 + \omega_y^2 y^2 + \omega_z^2 z^2) \right]. \quad (2.20)$$

Equation (2.20) offers us some insight as to how we can determine the chemical potential, knowing only information about the potential the atoms experience. From the normalization condition

$$1 = \int \int \int |\psi|^2 dx dy dz = \frac{8\pi}{15} \frac{\mu^{5/2}}{g} \sqrt{\frac{2}{M\omega_x^2}} \sqrt{\frac{2}{M\omega_y^2}} \sqrt{\frac{2}{M\omega_z^2}}, \quad (2.21)$$

where we can convert the square-root terms into a characteristic radius of the Gaussian ground state wavefunction for the given potential,  $a_{ho} = \sqrt{\hbar/M\omega}$ , by multiplying the top and bottom of the right side of the equation by  $\sqrt{\hbar}$  [18].

Multiplying both sides by the total number of atoms,  $N$ , yields something on left side that looks like  $N|\psi|^2$ . We understand the probability density to mean the distribution of where a particle is to be found in space and time[25]. Considering the addition of the all these distributions leads to a function that describes how many particles are to be found in a region space, a number density,  $n = N/\mathcal{V}$ . In the Thomas-Fermi limit it follows that the number

density for a condensate is

$$n(\vec{r}) = n_0 \left[ 1 - \frac{x^2}{R_x^2} - \frac{y^2}{R_y^2} - \frac{z^2}{R_z^2} \right]. \quad (2.22)$$

Here I have rewritten some of the terms in this equation to better highlight the ellipsoidal geometry of this number density function. We can see that the number density has a maximum at the center of the condensate, where  $n_0 = N\mu/g$  at the minimum of  $V$ . Similarly the width of the condensate in any one dimension is given by the Thomas-Fermi radii,  $R_i$ , from the equation  $\mu = \frac{1}{2}M\omega_i^2 R_i^2$ .

A distinguishing quality of this regime's number density, from the Gaussian form of the Maxwell-Boltzman distribution, is how the functional form of the Thomas-Fermi profile changes under integration. Where with a profile of the form  $n = n_0 e^{-\frac{x^2}{\sigma_x^2} - \frac{y^2}{\sigma_y^2} - \frac{z^2}{\sigma_z^2}}$  summing over one of its dimensions preserves its Gaussian structure, this is not the case with the Thomas-Fermi profile. Integrating once and twice we find[26],

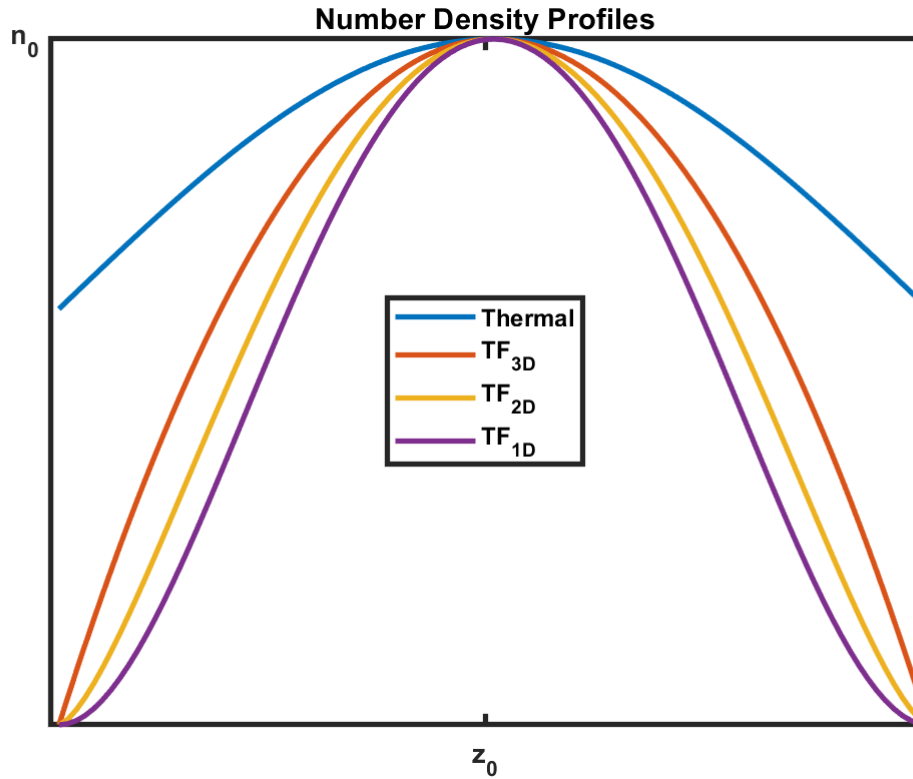


Figure 2.2: Distinctions in functional form between a thermal profile and three Thomas-Fermi profiles, integrated once, twice, and thrice.

$$n_{2D}(y, z) = \frac{4}{3}n_0R_x \left[ 1 - \frac{y^2}{R_y^2} - \frac{z^2}{R_z^2} \right]^{3/2}, \quad (2.23)$$

$$n_{1D}(z) = \frac{\pi}{2}n_0R_xR_y \left[ 1 - \frac{z^2}{R_z^2} \right]^2. \quad (2.24)$$

These result become important in the context fitting number density profiles to  $2D$  images of condensates and  $1D$  slices taken from those images, discussed in Section 4.2. Figure 2.2 is a comparison of the shape between the three different Thomas-Fermi profiles described in equations (2.22), (2.23), and (2.24), and the thermal number density profile for atom in the Maxwell-Boltzmann regime. All four equations have the same peak, center, and radial width.

## 2.3 Rubidium-87

In this section I will cover the relevant background of the atom we choose for experimentation. The nature of Bose-Einstein condensation is fundamental to all bosonic matter which behaves via the statistics described in first third of Section 2.1. In some sense the atom we choose should not matter in terms of the physics we are attempting to describe, so long as the composite of the atom's spin is of integer value. Within CAL's design, our apparatus has the capabilities to cool and trap isotopes of both rubidium and potassium, though our experiment solely employs the former[15]. It is evident at this point that some intrinsic features of the condensate are a function of properties related to the species of atom, i.e. the  $s$ -wave scattering length  $a$ . For the state of  $^{87}\text{Rb}$  we use that length has a value  $a = 95.4a_0$ , where  $a_0$  is the Bohr radius[27]. In discussing how we both bring these atoms down into their condensed phase and subsequently image them, the implications of our choice in  $^{87}\text{Rb}$  become more relevant. We find ourselves bringing the atom into focus here, since in order to reach degeneracy, we must first account for the internal energy stored within the atom.

So far any mention of a particular atomic species has been limited to the alkali metals. Why this group? For one, the phrase “hydrogen-like” is a descriptor of the important physics. Each atom in this group has a single valence electron in its outermost shell, approximating to a two particle system composed of a single  $-e$  particle surrounding around a core with

charge  $+e$  through the central field approximation[18]. The Schrödinger equation describing the potential exerted upon this valence electron therefore always yields an analytic solution. Furthermore from experiment we know atoms like potassium and rubidium to have larger scattering lengths than the likes of hydrogen[28, 29]. This provides us with one sufficient reason to choose rubidium as the strong degree of interaction between low energy atoms helps to justify the Thomas-Fermi approximation we made in the previous section further giving us an analytic solution to the Schrödinger equation describing the particle in an external system.

Another reason we choose rubidium is a matter of practicality. As we'll see in the next section our ability to cool an atomic vapor depends in part on our abilities to produce laser light at frequencies resonant with the internal energy structure of the atoms. The transition we drive in  $^{87}\text{Rb}$  increases the angular momentum of the valence electron, pushing it into the atom's  $p$ -orbital. This transition happens when the atoms are in the presence of light with  $\lambda \sim 780$  nm, or  $\omega \sim 2\pi \cdot 384$  THz[30]. In practice we are fairly capable of producing lasers emitting light at this wavelength. In fact CD players at the beginning of the 21<sup>st</sup> century used diodes of this frequency, leading physicists racing to create the earliest BECs to buy them wholesale[31].

In addition to detailing a single transition of the orbital angular momentum of the atom's valence electron, in Figure 2.3 we see the hyperfine splitting of these energy levels due to the electrons coupling with the nuclear magnetic dipole moment. When there isn't a strong external magnetic field affecting the electron, then the magnetic moment of the nucleus dominates and  $|F, m_F\rangle$  are the eigenstates of the system. The selection rules for transitions between these states requires that  $\Delta F = 0, \pm 1$  and  $\Delta m_F = 0, \pm 1$  from conservation of angular momentum. In the next section we discuss the applications of driving specific transitions with electromagnetic radiation for the purposes of cooling an atomic cloud. While we can drive specific  $\Delta F$  with polarized laser light, in the spontaneous emission of photons that happens thereafter  $\Delta F$  is random within its set of possible values. A particular optical pumping scheme, in our case to cool  $^{87}\text{Rb}$  into the ( $F=2$ ) hyperfine level of the ground state, will usually require more than a single laser to assure that there isn't sufficient loss from the effects of these selections rules.

A weak external magnetic field, when compared with the relative strength of the nuclear magnetic momentum, lifts the degeneracy of each hyperfine  $m_F$  state.  $^{87}\text{Rb}$  atoms pumped in

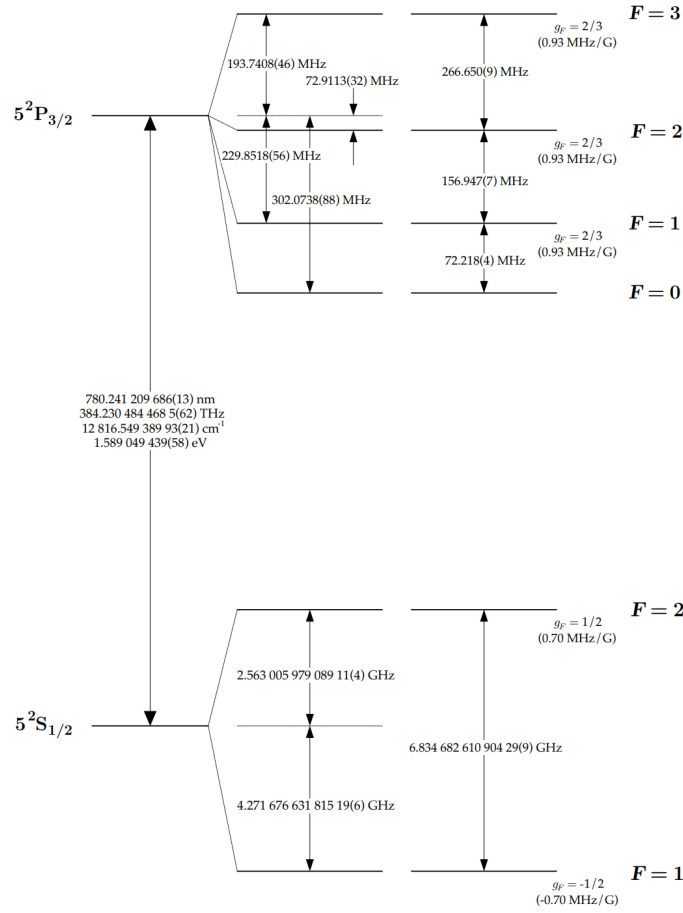


Figure 2.3: Hyperfine energy structure of  $^{87}\text{Rb}$  in the  $l=0$  and  $l=1$  states of the  $n=5$  energy level. The  $5^2S_{1/2}(F=2)$  level is the ground state we cool the atoms into in experiment. This notation, known as spectroscopic notation, works in terms of the more commonly used signifiers,  $n, s, l, j$ , as follows:  $|n, s, l, j\rangle \iff n^{2s+1}l_j$ . We use the atomic orbital notation  $l = s, p, d, \dots$  here. [30].

to the  $S_{1/2}(F=2)$  level have five distinct states in this regime,  $|2, 2\rangle, |2, 1\rangle, |2, 0\rangle, |2, -1\rangle, |2, -2\rangle$ . When we discuss how to trap these atoms in a conventional magnetic potential in the next section, we will see that some atoms will experience a potential well where others will experience a “hump” as a result of the possible  $m_F$  quantum numbers. We can take advantage of this to further cool the atomic cloud through the application of a time-dependant magnetic field in resonance with the splitting caused by the confining field. Turning this field on for a period of times drive transitions between all  $m_F$  states at once, pushing all atoms above a certain energy in their confinement into anti-trapped states. This is further quantified in the next section. The final condensate we then study is a collection of  $^{87}\text{Rb}$  atoms in  $|2, 2\rangle$  of their internal energy structure and the ground state of the confining magnetic potential.

Lastly of note, the isotope of rubidium we are experimenting upon does not naturally



occur in pure chunks. Lumps of this metal found in the Earth's crust are a mixture of approximately 25%  $^{87}\text{Rb}$  and 75%  $^{85}\text{Rb}$  isotopes, however as the internal energy structure of the latter isotope has different resonant frequencies for both optical and RF transitions its presence in the hot thermal cloud plays little role in the process of cooling. Additionally  $^{87}\text{Rb}$  experiences mild radioactive decay with a half-life of  $\sim 49$  billion years.

## 2.4 The Trapping and Cooling of Atoms

In this section I will cover the techniques implemented in experiment to produce Bose-Einstein condensates. For brevity, I will focus on only what is relevant to the cooling and trapping of atoms aboard CAL: the processes of laser cooling and evaporative cooling. Additionally there are a few theorems from the greater periphery of physics of which I will make reference to without prior discussion. There are a multitude of texts that encompass much more of our understanding of microscopic cooling than can fit here [18, 19, 20]. Ongoing research advances our abilities for how we can further cool atoms already trapped in adiabatic potentials [1, 32]. A specific confining potential we attempt to induce is discussed in section 3.3.

All of the work surrounding this field hinges upon two core concepts: 1.) the interaction of an oscillating electromagnetic field, i.e. light quanta, with atoms, and 2.) the interaction of a static magnetic field with atoms. We find a constant interplay between these effects in both of the cooling techniques the CAL apparatus utilizes. Rather than deriving each on their own, I will describe the physics of the devices that implement these techniques in our apparatus.

In experiment, when we first produce a hot atomic vapor we understand it to have the full distribution of Maxwell-Boltzmann velocities, a direct result of the kinetic theory of gases [17]:

$$f(v) = \left[ \frac{m}{2\pi k_B T} \right]^{3/2} e^{\frac{-m|v|^2}{2k_B T}}. \quad (2.25)$$

As we have seen briefly in Section 2.1 this distribution gives us a number density for a thermal cloud that is also Gaussian. We will see that this comes from the time evolution of the gas in free-fall in Section 2.5. Furthermore, the reference to temperature in this distribution is our

first sign of its relationship to the velocity of atoms, and subsequently their position, in our thermal cloud. We can see this more clearly by considering the average velocity of a particle in the distribution, which we can calculate through the expectation value of  $v$ . We write,

$$\langle v \rangle = \left[ \frac{8k_B T}{\pi m} \right]^{1/2}, \quad (2.26)$$

indicating that  $v \propto \sqrt{T}$ . Cooling this gas as we understand it becomes a question of how we can decrease the average velocity of atoms in this distribution.

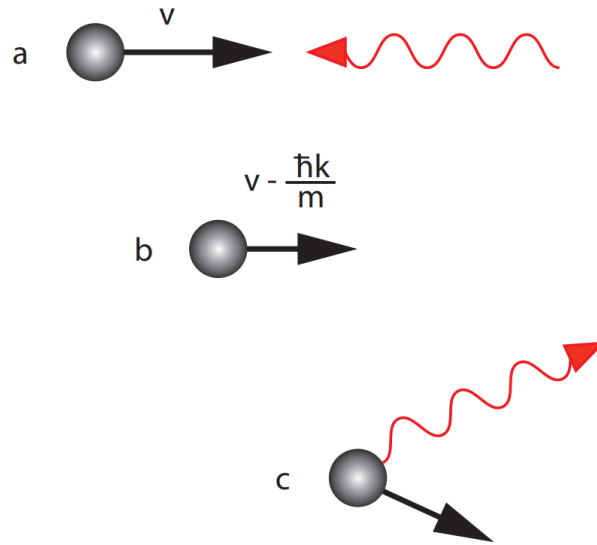


Figure 2.4: A diagram depicting the three fundamental steps of laser cooling. The excitation of the atom in a.) leads to a shift in its velocity related to the direction and momentum of the incoming photon as shown in b.). In c.) the atom re-emits a photon with the same momentum as the incoming one in a random direction and experiences a kick in the direction opposite of the emission. [33].

As mentioned above, our first tool to shrink this velocity distribution is the application of laser light. Laser cooling has existed in practice since the late seventies when the earliest demonstrations of a scattering force were first measured in experiment[34]. The idea that light carries momentum of  $\hbar k$  in discrete packets is one of our earliest results from quantum mechanics. Here  $k$  is the wavevector of the related electromagnetic wave description for light. Additionally we know atoms to absorb photons at certain frequencies,  $\omega_0$ , resonant with the internal energy structure of the atom, and then spontaneously reemit them in a random direction some time later. If an atom and a photon collide from counter-propagating trajectories, we can use conservation of momentum with the fact that the incoming photon no longer exists

to determine the change in velocity of the atom,  $\Delta v = -\hbar k$ . Likewise we can determine the effective change in magnitude of the atom's momentum when the photon is re-emitted.

One can ask the question of how the re-emission stage of the technique still works to shrink the atom's velocity distribution, if the atom then receives an additional kick of  $\hbar k$  in a random direction. This is where the collimation of light comes into play with the laser we are using to drive these transitions. We create a well collimated, effectively one-dimensional, stream of the thermal cloud through the use of a vacuum pump and a small nozzle. This means that we can quite effectively set up the laser cooling mechanism depicted above *ad infinitum*. The directionality here works not to shrink the overall velocity distribution of the atoms but to shrink the velocity distribution along the dimension of propagation that both beams point.

To take a slight detour: if we want to determine what the continuous application of a laser beam does to this component of the atom's velocity distribution, we need an understanding of the rate at which an atom will absorb and re-emit incoming photons. This is referred to as the scattering rate and is a result of calculating the Bloch density matrix of a mixed ensemble of excited and ground state atoms[19, 4]. It is given by:

$$R_{\text{scatt}} = \frac{\Gamma}{2} \frac{I/I_{\text{sat}}}{1 + I/I_{\text{sat}} + 4\delta^2/\Gamma^2}, \quad (2.27)$$

where  $\Gamma$  is the spectral linewidth of the transition, determining the range of frequencies capable of driving the atom to its excited state,  $I/I_{\text{sat}}$  is the intensity of the beam relative to an intensity at which the atoms spend half their time in the excited state, and  $\delta = \omega - \omega_0 \pm kv$  is the detuning of the laser. Here we use  $\pm kv$  to account for the Doppler shift of the atoms as they travel at  $v$ . For the case described above,  $kv$  is positive as the laser is counter-propagating the atomic beam. It follows that if an atom is constantly bombarded by laser light, it will experience a scattering force of,

$$F_{\text{scatt}} = \hbar k \cdot R_{\text{scatt}}. \quad (2.28)$$

Now we have tools to express the net effect of laser cooling on our thermal cloud.

How this all takes place inside CAL is via a laser cooling technique known as the magneto-optical trap (MOT). The MOT employs six counter-propagating laser beams directed on either

side of a point in the collimated stream of atoms, in all three of the principal dimensions. As in one dimension we can work to shrink the distribution of velocities, in all three we can shrink the average velocity of an atom in the distribution, effectively lowering the temperature of the ensemble. The random walk of the remission step is negligible in its effect on the atoms, as the sum of all those random directions adds up to nearly zero. In any one dimension the application of two laser beams works to create a scattering force  $F = F_{\text{scatt}}(\omega - \omega_0 - kv) - F_{\text{scatt}}(\omega - \omega_0 - kv)$ . Assuming that  $kv \ll \Gamma$  we can show that:

$$F = -\alpha v, \quad \alpha = -4\hbar k^2 \frac{I}{I_{\text{sat}}} \frac{2\delta/\Gamma}{[1 + (2\delta/\Gamma)^2]^2}. \quad (2.29)$$

Applying this to the other two dimensions as well shows that this technique works to drive a dampening force on the atoms in all directions, further demonstrating how this process shrinks the atom's velocity distribution. This technique alone is referred to as optical molasses and works to cool the thermal cloud, however the MOT takes this process a step further. By inducing a weak quadrupole trap, through for example two coils in anti-Helmholtz configuration, we can create a Zeeman splitting in the energy structure of atoms further from the center of the molasses. If the incoming laser light along a given axis is  $\sigma^\pm$  polarized, the correct polarization corresponding the  $m$  state with lower energy from the splitting, then as atoms travel further to the wings of the molasses they are more resonant with the incoming beam, which consequently drives more scattering back towards the center of the trap. The effect of this magnetic field

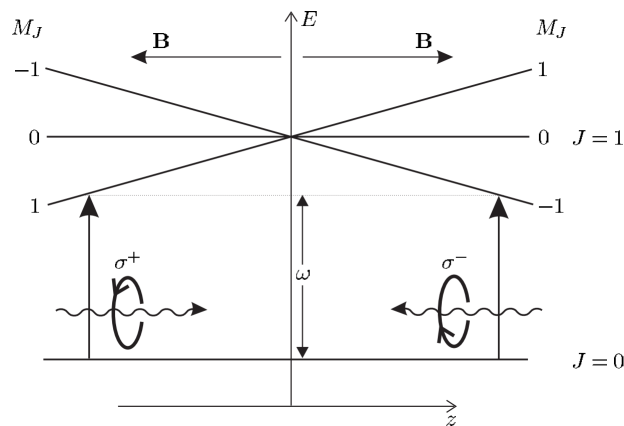


Figure 2.5: The simplest version of MOT for an atom with hydrogen-like weak-field Zeeman splitting. Atoms at points of higher field magnitude are more in resonant with the transitions driven by the polarized light coming from the MOT beams. [18]

works to create additional restoring component to the scattering force, as described below,

$$F = -\alpha v - \frac{\alpha\beta}{k}z, \quad \beta = \frac{g\mu_B}{\hbar} \frac{dB}{dz}, \quad (2.30)$$

again returning to a one dimensional case. The implication for the MOT is that while it is a tool to cool our thermal cloud, it also works to weakly confine atoms such to bolster the effects of an optical molasses.

If this technique provides cooling and confinement then why is not the only tool with which we bring bosonic atoms into their condensed phase? Then answer lies in a fundamental limit of laser cooling given by the equipartition theorem. A quick reminder of this theorem says that for any one dimension of motion,  $\frac{1}{2}Mv_z^2 = \frac{1}{2}k_B T$ . As we understand this velocity to be a function of  $R_{\text{scatt}}$ , we can determine a relation to temperature as,

$$k_B T = \frac{\hbar\Gamma}{4} \frac{1 + (2\delta/\Gamma)^2}{-2\delta/\Gamma}, \quad (2.31)$$

where the rightmost term has a minimum value of 2, when  $\delta = -\Gamma/2$ . This implies a lowest temperature that we can reach using this set of techniques, known as the Doppler cooling limit,

$$T_D = \frac{\hbar\Gamma}{k_B 2}. \quad (2.32)$$

For the  $^{87}\text{Rb}$  transition  $5^2S_{1/2}(F=2) \rightarrow 5^2P_{3/2}(F=3)$ , which has a spectral linewidth,  $\Gamma = 2\pi \cdot 6.065 \text{ Mhz}$ , we can determine a cooling limit of  $T_D = 146 \text{ } \mu\text{K}$ . This is not yet low enough for the atoms to condense into the ground state of their trap.

To further cool our collection of atoms we resort to confining them in a stronger potential. The principles of magnetic trapping have been in existence teasing out the quantum nature of thermal clouds long before we had the ability to bring hot atomic vapours into the low energy conditions where an atom's wavelike nature is measurable[35]. The potential atoms experience in the presence of an external magnetic field comes from the interaction of the field with the atom's magnetic dipole moment,  $\vec{\mu}$ ,

$$V = -\vec{\mu} \cdot \vec{B}. \quad (2.33)$$

If we recall that for the weak field regime the hyperfine structure of the atom still dominates, we can write this potential more explicitly as

$$V = g_F \mu_B m_F |\vec{B}|, \quad (2.34)$$

where  $g_F$  is the  $g$ -factor for this regime, and  $\mu_B$  is the Bohr magneton, which together make a unitary measure of the atom's magnetic moment. The quantum number  $m_F$  relates to distinctions in the orientation of angular momentum of the atom's valence electron, however without an external field present, as discussed in Section 2.3, these states are degenerate. For the hyperfine ( $F = 2$ ) ground state of  $^{87}\text{Rb}$ , the equation above relays that there are one of five distinct potentials the atoms will experience depending on their individual  $m_F$  state. Atoms with  $m_F = 0$  will experience no potential at all. The distinction in sign for the other possible values means that the minimums of some potentials are maximums for atoms in the other states. This becomes important in distinguishing how the trapping behavior of some atoms leads to anti-trapping behavior for others.

To trap the atoms we want a magnetic field that produces a potential well, however inducing this we lose atoms in states where  $m_F < 0$ , who experience a hump sending them out of the experiment. From Section 2.1, the trapping potential we used to define the parameters of our condensate state was a harmonic well. As it is the magnitude of the magnetic field that forms the shape of the potential, we don't need a magnetic field itself that is locally harmonic. Initially it would appear that any zero-crossing in the magnetic field would serve as a potential minimum for an atom in a positive  $m_F$  states, however these sub-levels become degenerate again at this minimum allowing atoms to transition out of the state in which they experience a trapping effect. In practice we have to do a little more to separate the potential minimum (or maximum) of each potential with the use of additional bias fields. In section 3.2, I will discuss how the CAL apparatus goes about producing this potential.

Let's now forget the  $m_F = 0$  and  $m_F = 1$  for a moment, which experience free-fall or a more relaxed well respectively. Consider the  $m_F = 2$  state, the collection of atoms we are trying to bring above a critical phase-space density. An atom with lower energy spends more time near the bottom of the well, whereas an atom with higher energy spends more time at

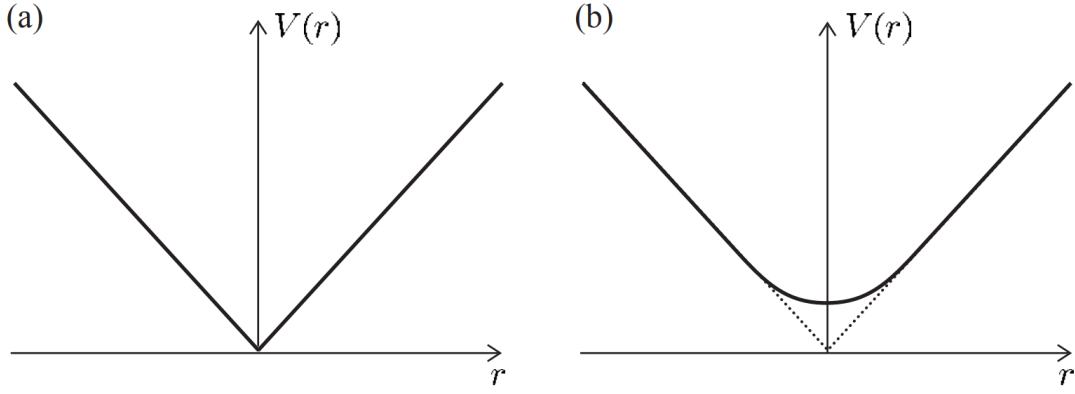


Figure 2.6: Conventional magnetic potentials with a.) adiabatic loss at the trap center and b.) a bias field working to create locally harmonic nonzero center.[18]

points higher up in the trap. Cooling as we have considered it thus far has been the lowering of the average energy of a particle in the system. If we want to further cool this thermal cloud one way is to remove these higher energy atoms, taking advantage of the locations we might find them in.

Useful to us is the idea that these higher energy atoms also exist at points of stronger fields meaning that their internal energy structure is split further in frequency space. This means that we can think of  $\Omega_0$ , describing some resonant frequency between  $|2, 2\rangle$  and  $|2, 1\rangle$ , that varies with position in the trap. Since the spacing between positional states of atoms in the trap is small compared to the spacing between  $m_F$  states, we can argue that this  $\Omega_0$  is also resonant with transitions from  $|2, 1\rangle \rightarrow |2, 0\rangle$  and  $|2, 0\rangle \rightarrow |2, -1\rangle$  states for atoms at specific energies experiencing those other potentials. If we turn some radiation on at this frequency for a period of time, atoms at resonant energies will slowly transition between all available  $m_F$  states before reaching one that induces an anti-trapping potential, sending the atom off and out of the experiment. In practice we use a magnetic field generated by a radio-frequency AC current. After a while the population of all states where  $m_F \geq 0$  decreases. The populations of  $m_F = 0$  and  $m_F = 1$  states approach zero, as these states are in weaker confinement leading more atoms to pass the point at which they are resonant with the radiation. Figure 2.7 is an image describing one path an atom could take out of the trap in this process. If in this time we sweep the frequency down over a small range resonant with atoms that have slightly lower energies, we chop off a larger fraction of the higher energy atoms. This is a technique in practice known as radio-frequency evaporative cooling, sometimes referred to as an RF knife,

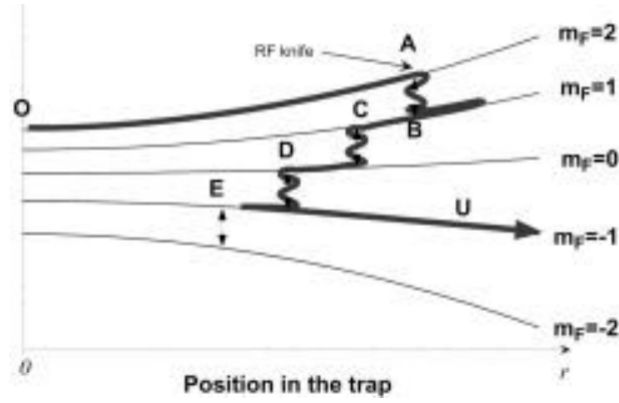


Figure 2.7: Radio-frequency evaporative cooling of  $^{87}\text{Rb}$  in a magnetic trap. If there is a probability  $P$  of the transition occurring at a point resonant with the RF radiation then the probability of an atom taking this path to leave the trap is  $P^3(1 - P)^2$ . There three other paths out of the trap that occur with the same probability[36].

and it effectively works to cool the distribution as it leads to an overall decrease in the average energy of an atom, after the cloud has re-thermalized at its new number.

Unlike with laser cooling, or Doppler cooling to more specifically categorize it in terms of its limitations, this technique can bring our thermal cloud well below the necessary critical temperature for it to transition into its condensate phase. Only when we lose the fine spacing of the energy levels of the trap in comparison to the  $m_F$  sub-level spacing do we see diminishing returns in our ability to cool. In other words when we really only have cold atoms left to remove evaporative cooling starts to present its limitations. The nature of what temperature we expect to find our atoms to reach degeneracy at I already have argued is more a result of their specific confinement, and rough predictions were made in Section 2.1. In Section 4.2 I go over how we determine an approximation of the cloud's final temperature to compare with these predictions.

## 2.5 Bose-Einstein Condensate Dynamics

This section briefly details the expansion dynamics of a condensate in free-fall. In Section 3.4 I will discuss the technique of time-of-flight (TOF) absorption imaging that we use to collect data on the condensates CAL produces. While we do not implement the set of equations,



characterized by Castin and Dum, they are important nonetheless as they convey that what we are looking at are not the original dimensions of our condensates[37].

Before presenting the expansion dynamics for a BEC, there is a useful result to take away from the classical expansion of a thermal cloud. If we recall the Maxwell-Boltzmann velocity distribution, it represents a probability distribution for the number of atoms at a given kinetic energy. In a potential well, like the traps discussed previously in this chapter, we understand that there is a relationship between energy and an atom's position in the trap. If we turn off the potential and allow the cloud to enter free-fall, it will expand to the effects of this velocity distribution. The fact that with CAL our free-falling cloud exists within an already free-falling frame means that we do not need to consider the additional expansion of the cloud along the  $z$  axis due to gravity. In the limit of a sufficiently long TOF we can justify that the relative difference of the initial positions of atoms before they expand is small compared to how far they have travelled thereafter. Therefore we can argue that  $x \sim vt_0$ , where  $t_0$  is the time constant of the TOF. Substituting this into Equation (2.1), and multiplying by  $N$ , we can write a number density distribution that is in terms of position:

$$n_{\text{TH}}(x, y, z) \cong N \left( \frac{m}{2\pi k_B T} \right)^{3/2} e^{-\frac{m(x-x_0)^2}{2k_B T \cdot t_0^2} - \frac{m(y-y_0)^2}{2k_B T \cdot t_0^2} - \frac{m(z-z_0)^2}{2k_B T \cdot t_0^2}}. \quad (2.35)$$

This equation becomes useful when attempting to fit our data to a thermal profile in long TOF. This is discussed further in Section 4.2.

The expansion of a condensate can be characterized by a fractional dilation from the interaction energy between the atoms. The width of each  $R_i$  scales by a unique parameter for each principle dimension of the trap.

$$R_i(t_0) = \lambda_i(t_0) R_i(t = 0) \quad (2.36)$$

It turns out that we can treat this expansion classically[37]. From Newtons' laws we obtain a differential equation for this scaling parameter,  $\lambda$ ,

$$\frac{\partial^2 \lambda_i}{\partial t^2} = \frac{\omega_i^2(0)}{\lambda_i \lambda_x \lambda_y \lambda_z} - \omega_i^2(t) \lambda_i. \quad (2.37)$$

This equation was derived with respect to a time-dependant potential. In experiment we turn off the trap and allow the condensate to enter free-fall for imaging. As this turning off happens on an instantaneous timescale the condensate experiences a time-dependent potential which induces this expansion.

# Chapter 3

## Apparatus

The CAL apparatus in its entirety was designed to fit within the dimensions of a standardized EXPRESS Rack aboard the ISS. The Rack system itself is set of individually temperature controlled module housings that provide power and export data for a variety of experimental apparatuses in orbit[38]. Interfacing systems with these modules allows for the operation of devices such as CAL without the input of astronauts aboard the space station.

Inside the external housing of CAL is a complex weave of laser systems, tapered amplifiers, frequency locking systems, spectroscopy modules, and current drivers[39]. The nature of the compactness necessary for setting up CAL in its place in orbit is a relative implosion of space when compared to more a traditional experimental setup, and is partly why no image of the apparatus as a whole, labelling its many parts, is depicted here. Instead I will focus my discussion on CAL's science chamber and its components; this space alone is where our condensates are formed and destroyed. The chapter will then continue with how the cooling techniques discussed in Chapter 3 are employed in CAL's science chamber, before discussing the kinds of condensates we can create with it.

### 3.1 The CAL Science Chamber

The science chamber housed within CAL ostensibly takes up one third of the instrument's internal space. It is cased in a magnetic shielding that protects the experiment from related noise of other electronics within the apparatus and the space station as a whole. A hot stream of atoms are pumped into the lower portion of the chamber in which they are transversely cooled and driven upward by a 2D MOT, utilizing a permanent magnet at the base of the chamber to set up the restoring component of the scattering force. The upper portion of the science chamber is a commercially sold RuBECi vacuum chamber designed by ColdQuanta, with added modification for CAL's purposes and the ability to study  $^{39}\text{K}$  and  $^{41}\text{K}$  BECs[15, 40]. At the top of the chamber is the apparatus's silicon atom chip chemically fused to be the topmost wall. Just exterior to the side walls of the chamber are two sets of anti-Helmholtz coils wound in rectangular loops. One set works to induce the restoring component for a 3D MOT. The other set of perpendicular coils are used to create an additionally quadrupole trap for transferring the atom cloud into the chip trap. The overlap of the field between the 3D MOT coils and these transfer coils allows us to reduce heating when bringing the cloud closer to the chip[15].

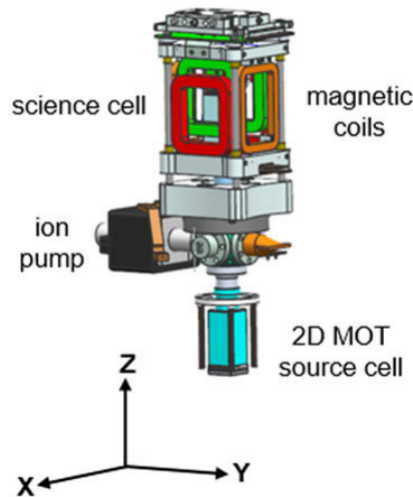


Figure 3.1: Interior of the CAL science chamber. The principle axes of the 3D MOT are depicted in the lower corner. Not shown is the science chamber's magnetic shielding and the mirrors directing the various beams used in each MOT[15].

## 3.2 The Atom Chip

The atom chip serves as CAL’s primary tool for evaporatively cooling the atoms down into their condensed phase. Chip traps were first implemented in the study of Bose-Einstein condensates in the early 2000s, with work demonstrating faster production times of condensates in tight confinements with long lifetimes[41, 42]. More recently atom chips, similarly designed by ColdQuanta, have been shown capable of producing condensates in as little as a single second[43]. The chip itself is fabricated through electron-beam optical lithography producing a patterned set of wires printed into a silicon base. It is then melded to an open face in the glass structure of the RuBECi vacuum chamber forming its sixth wall. The wires themselves are made of gold. This is due to its high reflectivity for the frequencies of light used in the optical transitions of the alkali metals used in experiment[44]. Maximum currents of up to 3 A have been measured for the individual pins of chips fabricated through similar means[40]. The wires that produce the trap in the center of chip can be the culmination of currents from several of these pins. The limited power constraints of the chip allows for the simultaneous

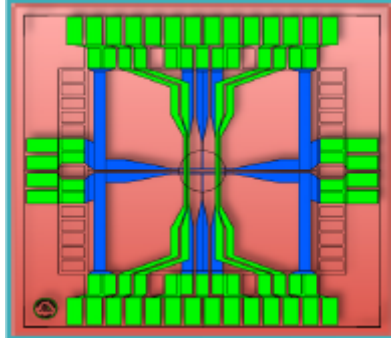


Figure 3.2: Layout of the wire configuration on the surface of the atom chip. Green rectangles denote the pins from which current enters the chip. The relevant “dimple” pattern used in the experiment exists within the center circle of the rendering[45].

manipulation of currents in the chip trap, the 3D MOT coils, and the transfer coils for a more tractable optimization of the overall cooling path[45].

The magnetic field produced by the wires in the chip do not act alone to the effect of trapping an atomic vapor. An additional uniform bias field for each of the principle axes of the chamber is added here, by the same coils which generate fields for the 3D MOT. The theory behind what’s effectively doing the the trapping stems from the “dimple” configuration of wires

on the surface of the atom chip, shown in Figure 3.3, where the resultant magnetic field in any

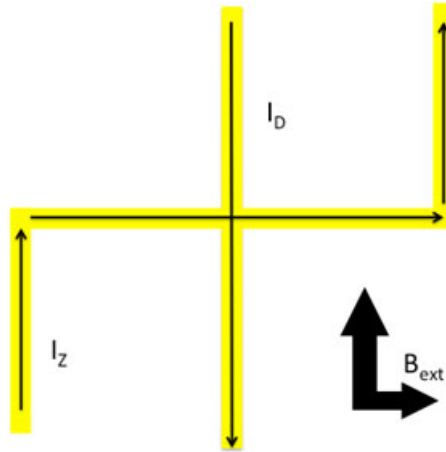


Figure 3.3: A rendering of the “dimple” trap wire configuration, as well as the direction of two applied bias fields [39].

direction above the surface of the chip decreases, as we move further away from the chip. The addition then of a strong, uniform external bias field works to create a minimum in the square of the magnetic field near the surface of the atom chip. From the physics of Section 2.4, this serves as a minimum energy point around which a fraction of the atoms become bound to a locally harmonic well. Examples of these potentials are shown later on in this section.

The trapped gas, still in a thermal regime, can be further cooled into a condensate through the evaporative cooling process of radio-frequency spin flip transitions of the hottest atoms to anti-trapped states, likewise discussed in Section 2.4. There exists a small loop of wire suspended above the atom chip through which we vary AC currents from  $\sim 30$  MHz to  $\sim 1$  MHz to achieve the desired transition of  $5^2S_{1/2}(F = 2, m_F = 2) \rightarrow 5^2S_{1/2}(F = 2, m_F = -1)$  in atoms at resonant points of the field, stepping through the two intermediary states along the way. Once we have initially cooled the gas below its critical temperature, we have a thin pencil-like condensate suspended roughly at  $z = 100 \mu\text{m}$ , above the surface of the chip[39]. Other applications of the RF loop are explained in the following section. It should also be noted that atom chips have been shown capable of employing evaporative cooling techniques for  $^{87}\text{Rb}$  through time-dependent microwave transitions as well as the brute force varying of chip currents directly, among other techniques[15, 46].

For the remainder of this section I will address the different trap configurations we employ

with CAL's atom chip and the predicted trap frequencies we expect from each configuration. The rendered images of these trapping potentials are produced via a model our lab uses in Mathematica[16]. The necessary inputs to produce the model are currents from the two wires in the “dimple” configuration as well as an additional bias field current for each of the principle axes. We use an extra parameter,  $\mathbf{f}$ , to scale the strength of each bias field on the interval  $[0, 1]$ . The initial tight trap has the full strength of this scaling parameter,  $\mathbf{f} = 1$ . In order to reach the weaker trapping configuration in which we experiment, we bring this parameter down to around one fifth of its initial value. By weakening the bias field we are able to translate the trap's center further away from the chip. The new potential also keeps the atoms in weaker confinement, this expansion leading to a colder condensate (in a trap with a lower  $T_c$ ). The possibility of heating incurs through both of these coinciding motions. The ramp therefore must be done very slowly if we want to preserve the condensate. Some effects of this ramp are discussed in Chapter 4.

The tight trap we model has characteristic frequencies nearly an order of magnitude higher in the dimensions with the tightest confinement, when compared to the frequencies of our final traps. While the currents inducing the fields of the tight trap are unique to the final trapping configuration, the relative strength of the initial  $z$  bias field allows our condensates to begin in similar pencil-like confinement for all final configurations. Figure 3.4 is an example of the field magnitude in all directions for this tight trap. On the left is the potential on the  $z$  axis, whereas the right shows the two transverse axes (the green:  $\vec{\parallel}$ ; the orange:  $\vec{\perp}$ ).

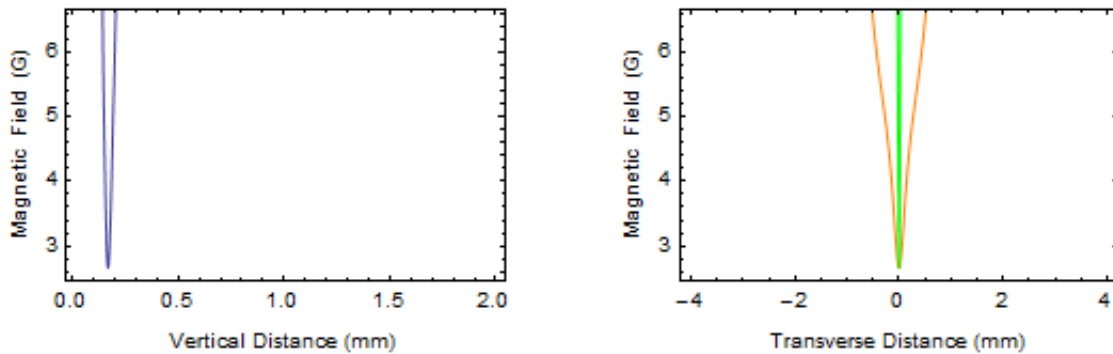


Figure 3.4: Tight trap with fields from trapping configuration 2 [16]

From the data we have taken so far, there are currently two final trapping configurations

we can characterize. These potentials are those produced by ramping down the strength of the bias fields to a weaker confinement, positioning the trap further from the atom chip. The former of the two is slightly tighter than the latter on the  $z$  axis, among other dimensions. This leads to slightly higher predicted characteristic frequencies:  $\omega_{\parallel} = 2\pi \cdot 31.5$  Hz,  $\omega_{\perp} = 2\pi \cdot 98.4$  Hz,  $\omega_z = 2\pi \cdot 100.8$  Hz. The second trapping configuration has a weaker confinement. Our

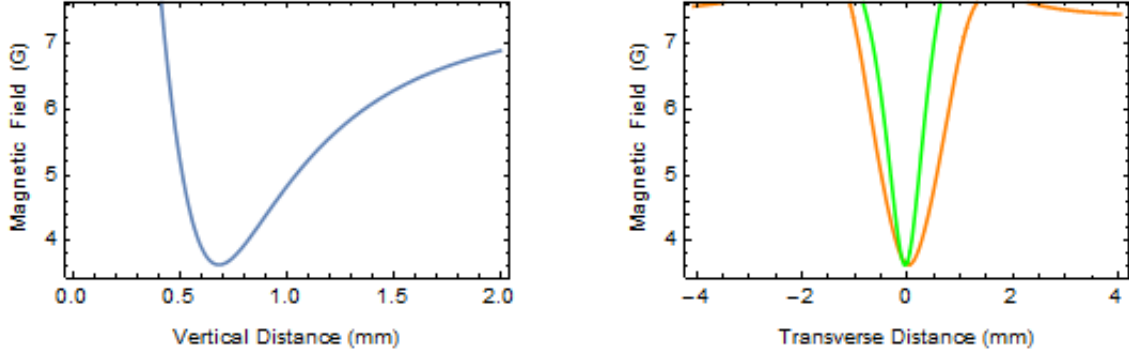


Figure 3.5: Final trapping configuration 1 [16].

predictions are:  $\omega_{\parallel} = 2\pi \cdot 25.9$  Hz,  $\omega_{\perp} = 2\pi \cdot 87.3$  Hz,  $\omega_z = 2\pi \cdot 87.1$  Hz.

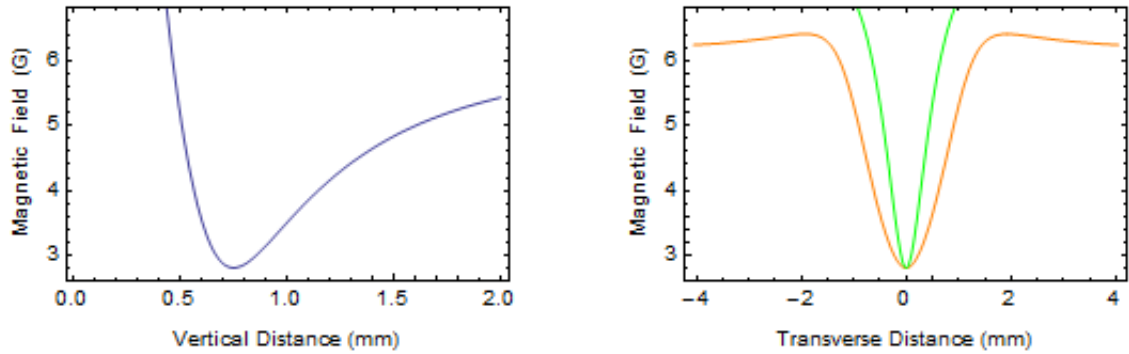


Figure 3.6: Final trapping configuration 2 [16].

### 3.3 Radio-Frequency Dressing

As mentioned above, the apparatus utilizes a small loop of wire, 10 mm in diameter, for driving radio-frequency transitions among atoms in the trap[15]. Additionally there exists an outer loop of wire, 12.5 mm in diameter, for microwave frequency currents applied in K



experiments and alternate cooling schemes for Rb[15]. For the experiments presented within this thesis this microwave loop is not used. Figure 3.7 is an image of both wire antennae housed within the RuBECi chamber. In Section 2.4, I discussed how tuning the RF antenna

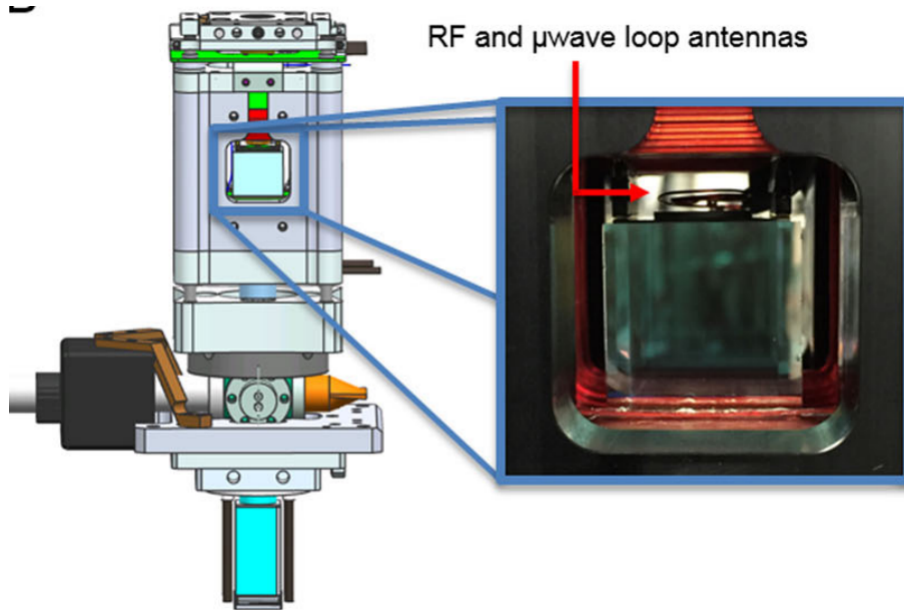


Figure 3.7: Depiction of the RF and  $\mu$ F wiring used both for the purposes of evaporative cooling and dressing potentials. [15].

in resonance with atoms at high fields in the trap can be applied to drive the hottest portion of atoms in the gas to their anti-trapped states. Now I will describe how we can apply RF frequencies to achieve unique potentials discussed in the introduction, in which we aim to study condensate behavior in the future.

The process of RF-dressing to produce a bubble trap involves the ramping of a radio-frequency magnetic field, the same as with evaporative cooling, however this time taking a “bottom up” approach. We sweep from a frequency detuned below resonance with atoms at the minimum of the trap. Ramping the frequency upwards slowly transitions atoms into a superposition of trapped and anti-trapped states, causing the atoms to live at points of lowest potential in the superimposed state (depicted in rightmost image of Figure 3.8). The detuning and slow ramp of this process are crucial in order to maintain adiabaticity in the transition from the standard magnetic potential to the dressed one[1]. Without these features, the process of RF-dressing threatens the condensate state of the trapped gas in creating additional heating. Figure 3.8 contains a series of images detailing the transition to a dressed trap. Once the trap

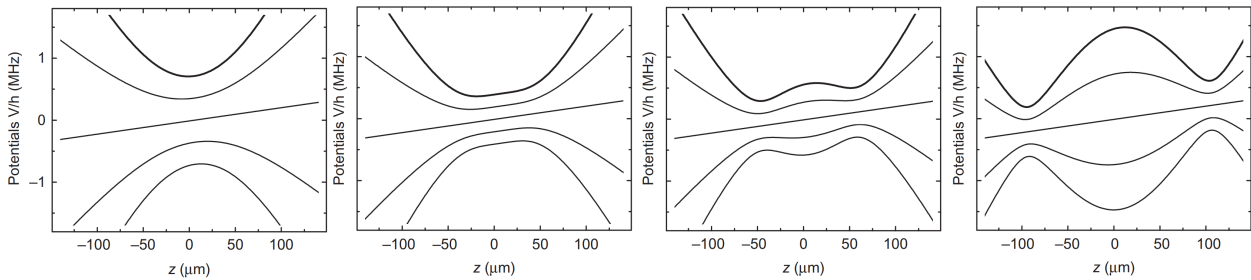


Figure 3.8: Depiction of transition from a conventional magnetic trap to one that is radio-frequency dressed. Note the slope in  $z$  conveys the root of the terrestrial sagging effect realized in the application of this potential terrestrially[1].

is formed atoms in their condensed phase are dislocated from the conventional trap center and live at points of higher magnetic field. If we apply this potential in all dimensions, one can imagine the ellipsoidal shell of condensed atoms created in this process of RF dressing. As we sweep the frequency higher we project a shell that is thinner.

Of note is that the image above depicts a dressed potential constructed terrestrially, hence the tilt of each potential. This tilt applied to the potential by gravity works to create a sagging effect in the bubble condensate produced via this dressing method on Earth[5]. This sagging has been applied in a number of terrestrial experiments to produce quasi-2D condensate, but never as a fully closed shell[8, 47, 48]. This is the crucial role that CAL's position in free-fall plays in helping us work towards the construction of a hollow condensate. In orbit around the planet, we are able to produce dressed potentials without a slanted potential in one dimension. It is of significant note that the characterization of the final undressed trap configuration plays an important role in mapping out how we can adiabatically perform this dressing. We need to know the exact structure of our conventional trap before we can effectively apply this dressing.

### 3.4 Imaging

After the ramp of the bias field into the experiment's final trapping configuration the condensate resembles an ellipsoid. In order to image, we turn off all fields and the allow the condensate to enter a time-of-flight (TOF) free-fall. Where on Earth the condensate would descend out of the frame of the camera, the microgravity environment made available to us

with CAL allows the condensate to remain roughly in the same spatial location for both short TOF and long TOF. The variation of TOF that exists in the experiments presented within this thesis are on the order of ms, ranging from 4 – 30 ms.

A probe beam, tuned in resonance with the  $5^2S_{1/2}(F=2) \rightarrow 5^2P_{3/2}(F=3)$  transition, is then turned on creating a shadow of absorption over the position of the condensate. The condensate is imaged by a CMOS camera, opposite the probe, with a pixel size,  $p_{\text{eff}} = 4.51 \mu\text{m}$ , scaling the distance between the cloud's position in pixel space and the value we report for its center[49, 15]. The atoms in the condensate having absorbed the incoming light of the probe are excited out of their ground state. The condensate is consequentially destroyed in this imaging process, allowing us to easily take an additional image of the frame without the shadow present in order to compare with the absorption image. In Figure 3.9 I present examples of both absorption and empty raw images taken with CAL. The images are processed, per each

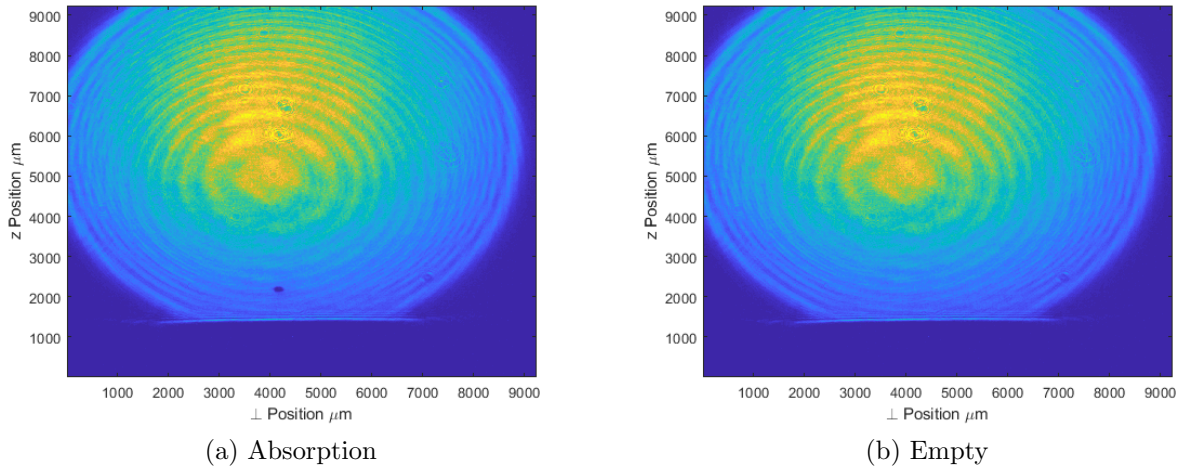


Figure 3.9: Raw images of (a) the absorption image and (b) the empty image for a  $5^2S_{1/2}(F=2, M=2)$   $^{87}\text{Rb}$  condensate in the first trapping configuration,  $t_0 = 4$  ms. Note that the flat dark cutoff of each image is the base of the atom chip, found to be at height of  $z = 1389 \pm 9 \mu\text{m}$  from the base of the camera's frame.

shot, using the natural logarithm of the ratio of intensities over the  $\perp$  and  $z$  components of the two images. This allows the neutralization of background noise as it is understood to not significantly change in the time of imaging, resulting in low to zero values where the cloud is not present.

The two dimensional nature of this imaging lends itself nicely to a coordinate system of unit vectors,  $\hat{\perp}$ ,  $\hat{\parallel}$ ,  $\hat{z}$ , with  $\hat{z}$  describing the vertical direction. This notation will be used for

the remainder of this thesis. The resultant data is in units of optical depths denoted by  $\mathcal{OD}$  in the definition,

$$\mathcal{OD}(\perp, z) \equiv -\ln \frac{I(\perp, z)}{I_0(\perp, z)} \quad (3.1)$$

where  $I$  and  $I_0$  are intensities of the shadow image and empty image respectively. This value is useful to us as it is proportional to the number density,  $n$ , of the condensate in the frame of the camera. Additionally optical depths are unitless. As light is absorbed along the axis of propagation for the probe, the shadow image is proportional to an integral over the density of atoms in the column space of each pixel, given by,

$$\mathcal{OD}(\perp, z) = \sigma_0 \int n(\perp, \parallel, z) d(\parallel), \quad (3.2)$$

where  $\sigma_0$  is absorption cross section, discussed further in Section 4.2. Information about the distribution of atoms in the space along the axis of imaging,  $\hat{\parallel}$ , is lost using this method, although we do suspect its ellipsoidal geometry to carry over in this third dimension, in line with the predication made by the trap configuration models discussed in section 3.2. Figure 3.10 is a processed image of  $\mathcal{OD}$  for a condensate in the first trapping configuration, in short TOF.

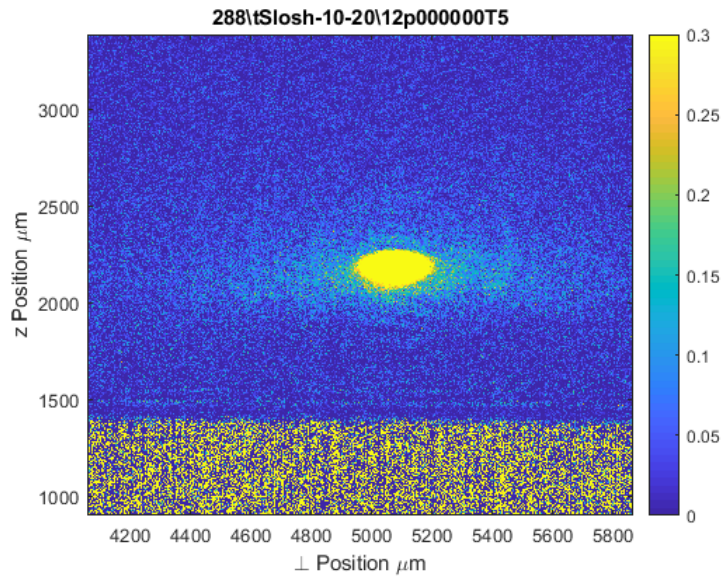


Figure 3.10: The processed image of the condensate from the previous figure. Note: The background evaporative halo is not related to the re-thermalization of the condensate, as the TOF is too short for it to have a visible thermal component. The root of this halo is discussed in Section 4.3.

# Chapter 4

## Analysis

This chapter covers the range of experiments we have performed thus far with CAL. I present some analyses of attempts at adiabatic ramps, however the predominate significance of this section is the characterization of frequencies for the first and second trapping configurations that we study atomic clouds within. All experiments with CAL utilize time-of-flight (TOF) imaging, however these characterization trials introduce an additional parameter time-in-trap (TIT) that allows us to construct a beautiful map of the condensate's trajectory as we swish it back and forth in its potential like a bowl of soup. I will discuss how we do this in more depth in Section 4.4.

Essential to the efficacy of these analyses are a number of custom fits built in MATLAB from the theory discussed in Chapter 2. I will revisit the Thomas-Fermi approximation we made in Section 2.2 in order to explain the physical parameters we can extract from images alone of these clouds. The transition in geometry that occurs when we integrate across our image becomes central in the discussion of how we determine the number of atoms in our condensate.

Lastly some experiments are presented in which we experience significant error from our predictions. Relevant sources of error are discussed in Chapter 5.

## 4.1 Overview of Code

In Section 3.4 I discussed how the raw images taken by CAL are processed in MATLAB via a ratio of optical depths,  $\mathcal{OD}$ . In this section I will discuss the operations we perform on the processed image to excise a smaller frame around the cloud for further analysis. In the images of the condensates presented within this section we scale color to  $\mathcal{OD}$  on an interval of either  $[0, 3]$  or  $[0, 4]$ , as optical depths above  $\gtrsim 3.5$  represent saturation. Saturation occurs from the finite amount of laser light that is produced by the laser diode off resonance with condensate due to imperfections in the laser[50]. This leads the camera to register more light in the raw absorption image, artificially lowering  $\mathcal{OD}$ . I at times also scale color on a much smaller  $[0, 0.3]$  interval, in order to highlight the presence of atomic matter in any state.

An additional source of distortion in  $\mathcal{OD}$  comes from the physical presence of the atom chip in the frame of the image. Taking the optical depths for regions of the image in which the laser is diffracting off of or blocked by the chip leads to a substantially increased level of noise. In order to separate these regions from our fitting analysis, we excise a rough rectangle around the condensate (or thermal cloud) of an arbitrary size to perform a center-of-mass calculation. This helps to produce an approximation of the cloud's center, which we utilize to fix an ever smaller frame ( $401 \times 401$  pixel) we excise to perform the fit on. The rest of the code consists of a series of 1D fitting routines that we use to determine the size, optical density, and position of the condensate to a sufficient degree with which we can see the physical constraints of our

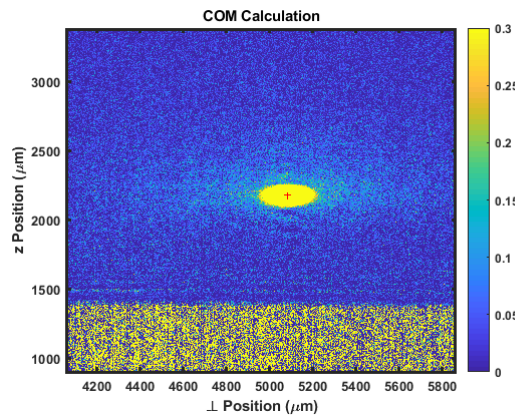


Figure 4.1: COM calculation (in an arbitrary frame) denoted by the red "+". Again note the presence of a large halo in the background of the condensate discussed in Section 4.3.

atomic system. As our COM calculation is only a rough estimation however, we do not use it to orient the fit. Instead we sum over the perpendicular dimension (perpendicular referring to the dimension we are not attempt to fit to) and concatenate information about the condensate into an array that is a measure of total optical depths in each row of the image. This allows us to condense our images into a 1D form. We benefit in that we no longer need information about  $\perp_0$  when fitting to a  $z$  profile and vice versa. Our data then is no longer proportional to optical depths but to the column sum of optical depths, which I denote as  $\mathcal{OD}_{\text{sum}}$ . Here I will create the distinction between a 1D *sum* and a 1D *slice* in whether we are looking at a density profile that is summed along its perpendicular dimension versus one that is a slice through this perpendicular dimension. While we perform our fits on the former data, we extrapolate information from this fit to construct functions of the latter.

## 4.2 Fitting Center, Number, and Temperature

This section describes how I arrive at the functional forms of the fits I use in analysis of these images. In returning to the theory of the objects that we are studying I will demonstrate relationships between our fitting parameters and the physics of the atomic clouds we are studying. Later on in this section I share a few examples of some fits that capture number and temperature for these atomic clouds. At the end of this section I look at a histogram for atom number in short TOF and present a partial set of fits from the experiment discussed in Section 4.4.

In Chapter 2 we expressed ways to relate the physical properties of both thermal clouds and condensates to the geometry of their respective number densities,  $n$ . Abstracting those equations into simpler forms provides us with a set of coefficients we can find from performing a linear least squares (LLS) fit of our optical depth data. I will now discuss the fit I use in my software and how I estimate temperature and number for the images we analyze. Below I restate the  $n_{3D}$  profiles for both a thermal cloud and a condensate approximated in the Thomas-Fermi regime and demonstrate the first level of integration that brings our number



densities into proportionality with optical depths. For a thermal cloud we observe in our image

$$n_{\mathbf{TH}} \cong N \left( \frac{m}{2\pi k_B T} \right)^{3/2} e^{-\frac{m(x-x_0)^2}{2k_B T \cdot t_0^2} - \frac{m(y-y_0)^2}{2k_B T \cdot t_0^2} - \frac{m(z-z_0)^2}{2k_B T \cdot t_0^2}} \quad (4.1)$$

$$\rightarrow n_0 e^{-\frac{(y-y_0)^2}{2\sigma_y^2} - \frac{(z-z_0)^2}{2\sigma_z^2}} \propto \mathcal{OD},$$

where  $t_0$  is the time constant of the TOF. And for a cloud in the Thomas-Fermi regime we observe in our image

$$n_{\mathbf{TF}} \rightarrow n_0 \left[ 1 - \frac{(y-y_0)^2}{R_y^2(t_0)} - \frac{(z-z_0)^2}{R_z^2(t_0)} \right]^{3/2} \propto \mathcal{OD}. \quad (4.2)$$

where each  $R_i(t_0)$  is the dilated Thomas-Fermi radius from Equation (2.36). In each equation we now have set of parameters describing the peak of the cloud's density profile,  $n_0$ , the cloud's center along a given axis,  $i_0$ , and the cloud's radial TOF width along that axis,  $\sigma_i$  or  $R_i$ . We add an additional constant  $+N$  (to distinguish it from  $N$ ) to determine a floor created by the level of background noise in the image. One of these functions we understand to have the shape of a Gaussian distribution; the other we recognize as the maximum of an upside-down parabola and the line  $i = 0$  for each dimension, integrated once. The peak density,  $n_0$ , of the profile relates our fitting function to the dimensional structure of our absorption imaging data, our measure of  $\mathcal{OD}$ . The fact that we take the first integral of the  $n_{3D}$  means that our data only reflects the fraction of atoms which absorbed photons during the span of the image and that the peak  $n_0$  has units  $\text{m}^{-2}$ . A 2D pixel that reports  $\mathcal{OD}/ps_{\text{eff}}^2$  will then only see

$$\frac{\mathcal{OD}}{ps_{\text{eff}}^2} \propto \frac{n_0 \sigma_0}{ps_{\text{eff}}^2}, \quad (4.3)$$

where  $\sigma_0$  is the absorption cross-section, which quantifies the probability of the interaction between a photon and an atom occurring. Explicitly,  $\sigma_0 = \hbar\omega_0\Gamma/2I_{\text{sat}}$  which for the  $^{87}\text{Rb}$   $S_{1/2}(F=2) \rightarrow P_{3/2}(F=3)$  transition (via  $\sigma^\pm$  light) has a value  $\sigma_0 = 2.9 \times 10^{-13} \text{ m}^2$  [49].

If we integrated Equations (4.1) and (4.2) we arrive at the functional forms I employ in our 1D fitting routines. Making the substitution  $y \rightarrow \perp$  and summing over this dimension we



see the two following equations (accounting for background noise):

$$\mathcal{OD}_{\mathbf{TH}, \text{Sum}\perp} = n_0 \sigma_0 e^{-\frac{(z-z_0)^2}{2\sigma_z^2}} + N, \quad (4.4)$$

$$\mathcal{OD}_{\mathbf{TF}, \text{Sum}\perp} = n_0 \sigma_0 \left[ 1 - \frac{(z-z_0)^2}{R_z^2} \right]^2 + N, \quad (4.5)$$

as well two equations with the coordinates reversed. Naturally, the value of  $n_0$  differs between Equations (4.1) and (4.4), and (4.2) and (4.5) respectively. The constant we summate in taking this integral is concatenated into the new  $n_0^{1D} = C \cdot n_0^{2D}$ , as our fit cannot distinguish between these coefficients individually from a measure of their product. Since we perform a fit of the 1D sums in both dimension of the image we can actually extrapolate back the two dimensional peak  $\mathcal{OD}$ . We find the estimate  $n_0^{2D}$  for a given dimension in the thermal case simply as

$$n_{z_0}^{2D} = \frac{n_{z_0}^{1D}}{\sqrt{2\pi}\sigma_\perp}. \quad (4.6)$$

For the Thomas-Fermi case I refer to equation Equations (2.23) and (2.24) to show that

$$n_{z_0}^{2D} = \frac{8\pi}{3} \frac{n_{z_0}^{1D} p_{\text{seff}}}{R_\perp}. \quad (4.7)$$

We then average of the result from both dimension to get a value for  $n_0^{2D}$  in either case. This value represents the peak we would find if we were to take a slice through the center of the cloud in the 2D frame. This calculation is referenced later on this section when I discuss how we determine atom number.

In general we fit data from a 1D number density profile to the bimodal sum of the two distributions described in Equations (4.4) and (4.5). As Equation (2.13) implies, at finite  $T < T_c$  there is a percentage of the atoms in the ground state and a percentage still occupying excited energy levels. Fitting to this bimodal distribution allows us to make a calculation of this fraction. However, the analysis presented in Section 4.3 discusses one unreliability of this form in the case of a short TOF. Even in long TOF current progress on my analysis involves making this calculation more accurate.

The main necessity of these fits is that both must be robust towards capturing the

cloud's center to a significantly high degree. If it is central to this thesis to capture the center-of-mass sloshing of a condensate in its harmonic trap then we need a determination of that center to a much higher degree than the COM calculation we made in processing the image. Both the Gaussian functional form of the thermal distribution and the parabolic form of the Thomas-Fermi distribution have well-defined centers that don't change when we integrate them. The LLS regression formula built into MATLAB is able to fit a center within  $6 \mu\text{m}$  with 95% confidence. Some of the fits presented in this thesis have a thermal and Thomas-Fermi component which appear out of phase. This is also discussed in Section 4.3. Some variation is

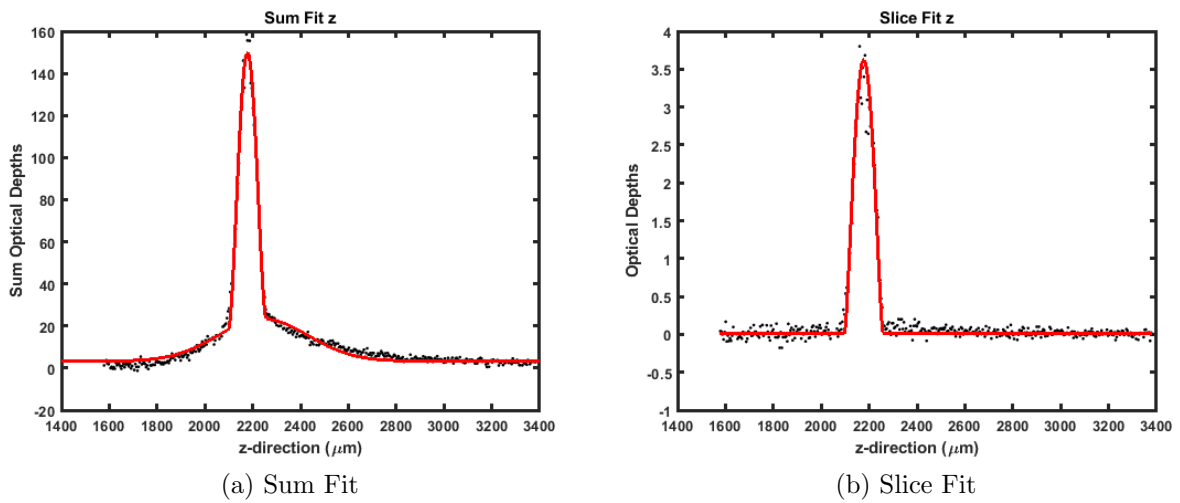


Figure 4.2: Example of (a) a fit over the sum of the perpendicular dimension and (b) a fit about a slice through the perpendicular center of the condensate. The condensate was ramped into the first trap configuration and released for a short TOF,  $t_0 = 4 \text{ ms}$ , before imaging. I report  $N \sim 140000$  for this image. The slight variation in phase of the two curves in (a) is discussed in Section 4.3. Data where  $\mathcal{OD} \gtrsim 3.5$  in (b) expresses saturated  $\mathcal{OD}$ .

noted between the fit and the data at the peak of each curve. This peak represents the intensity at which our measure of  $\mathcal{OD}$  becomes saturated. As the fit grabs onto a rough average of these peak values, the values I determine for  $n_0$  and subsequently  $N$  could serve as an underestimate.

From a fit of the form of Equation (4.4) we can get an estimate for temperature by approximating the whole cloud to a thermal distribution. There are two concerns with doing this however. For one, our original 3D thermal number density, in Equation (4.1), is only true in the limit of long TOF where the expansion of the cloud leads to the relation  $v \sim x/t_0$ . Secondly for images of partially condensed states with noticeable Thomas-Fermi components, fitting to only a thermal distribution artificially selects a thinner Gaussian than

the one describing whatever component of the  $\mathcal{OD}$  profile that is truly thermal (see Figure 4.3). Our best determination of temperature then comes from the width of the Gaussian component of our bimodal fit. Doing so is made easier by imaging in long TOF, allowing the thermal component to expand sufficiently from its tight confinement. We use the following equation to determine an estimate for both the  $\hat{\perp}$  and  $\hat{z}$  fits.

$$T = \frac{m\sigma_{\perp}^2}{k_B t_0^2}. \quad (4.8)$$

For most of the clouds analyzed within this thesis, I report a temperature in the range of  $\sim 110$ - $160$  nK for their thermal components. This a reasonable estimation based on the predictions we made for  $T_c$  in the final weak trap in Section 2.1. The confidence bounds for our fits of the Gaussian width are also decently small, however as  $T \propto \sigma^2$  a small error our measure of width can result in a significant miscalculation of the temperature. While our lack of current data in

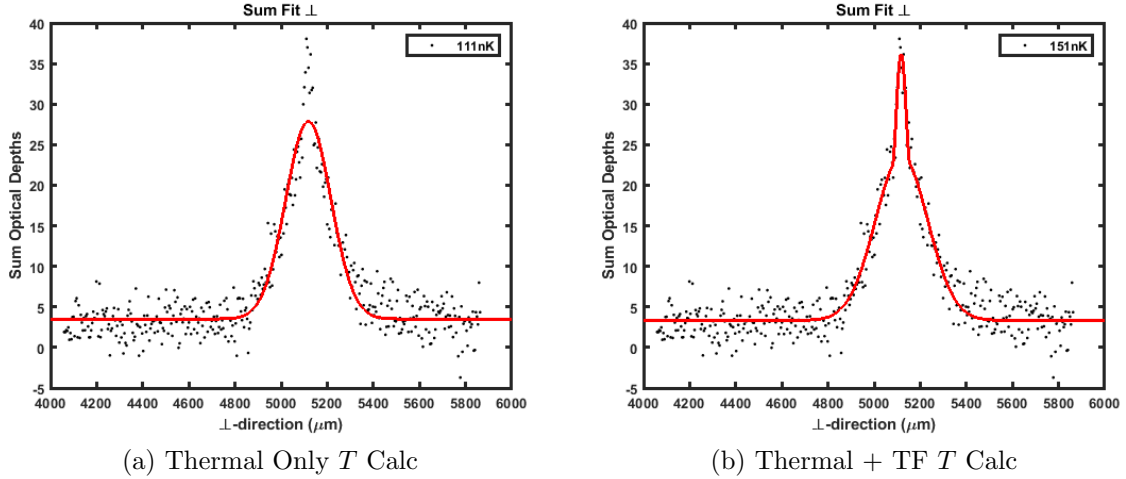


Figure 4.3: (a) Thermal fit to a 1D sum of a number density profile.  $t_0 = 30$  ms leading to a calculation of  $T = 111$  nK. (b) TF + thermal fit of the same density profile determining  $T = 151$  nK. The calculated ground state population for (b) was 44%, a number that seems exceedingly above what is observed. We can see how a slight change in the width of the Thermal component,  $\sigma_{\perp}$ , correlates to a sizable change in  $T$ . The fit's prediction is 95% confident in this width to  $\sim 6 \mu\text{m}$ .

long TOF with CAL serves to limit our capabilities to further develop the robustness of this temperature calculator, it still serves as a good in-house tool to compare estimations across the experiments I analyze. Further applications of this temperature calculator are discussed in Section 4.5.

A determination of atom number can be made one of two ways. A somewhat simpler way to perform this calculation is to sum over the all  $\mathcal{OD}$  with the fitted noise constant  $N$  subtracted everywhere from our measure. The equation for number then is

$$N = \frac{ps_{\text{eff}}^2}{\sigma_0} \sum_{\perp_i} \sum_{z_i} \left( \mathcal{OD}(\perp_i, z_i) - N \right) \quad (4.9)$$

Our ability to effectively calculate this noise threshold is the bar we face in performing this calculation. As the variation of  $\mathcal{OD}(\perp_i, z_i)$  is much rougher than our fitted curve, the number calculator serves at best as a ballpark estimate. We can with more accuracy determine a number from the relationship to peak number density that we expressed earlier on in this section. From a thermal distribution we can determine,

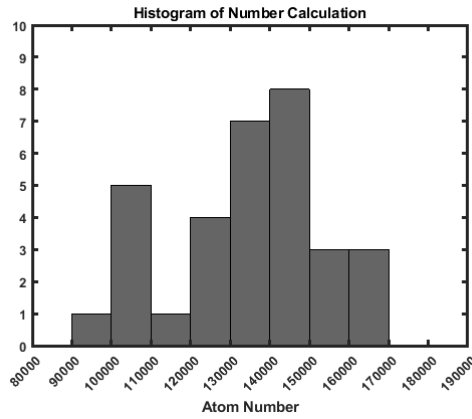


Figure 4.4: Histogram of atom number for the experiments discussed in Section 4.4. All are taken from trials with  $t_0 \sim 4$  ms.

$$N = 2\pi \frac{n^{2D}(\perp_0, z_0)}{\sigma_0} \sigma_{\perp} \sigma_z, \quad (4.10)$$

And for a Thomas-Fermi distribution,

$$N = \frac{2\pi}{5} \frac{n^{2D}(\perp_0, z_0)}{\sigma_0} R_{\perp} R_z. \quad (4.11)$$

Atom number can vary in experiment depending on thermal fluctuations in the apparatus as a whole. Our best estimates of  $N$  thus far comes from short TOF experiments, in which there is almost no visible thermal component. For these trials I report a range of atom numbers:

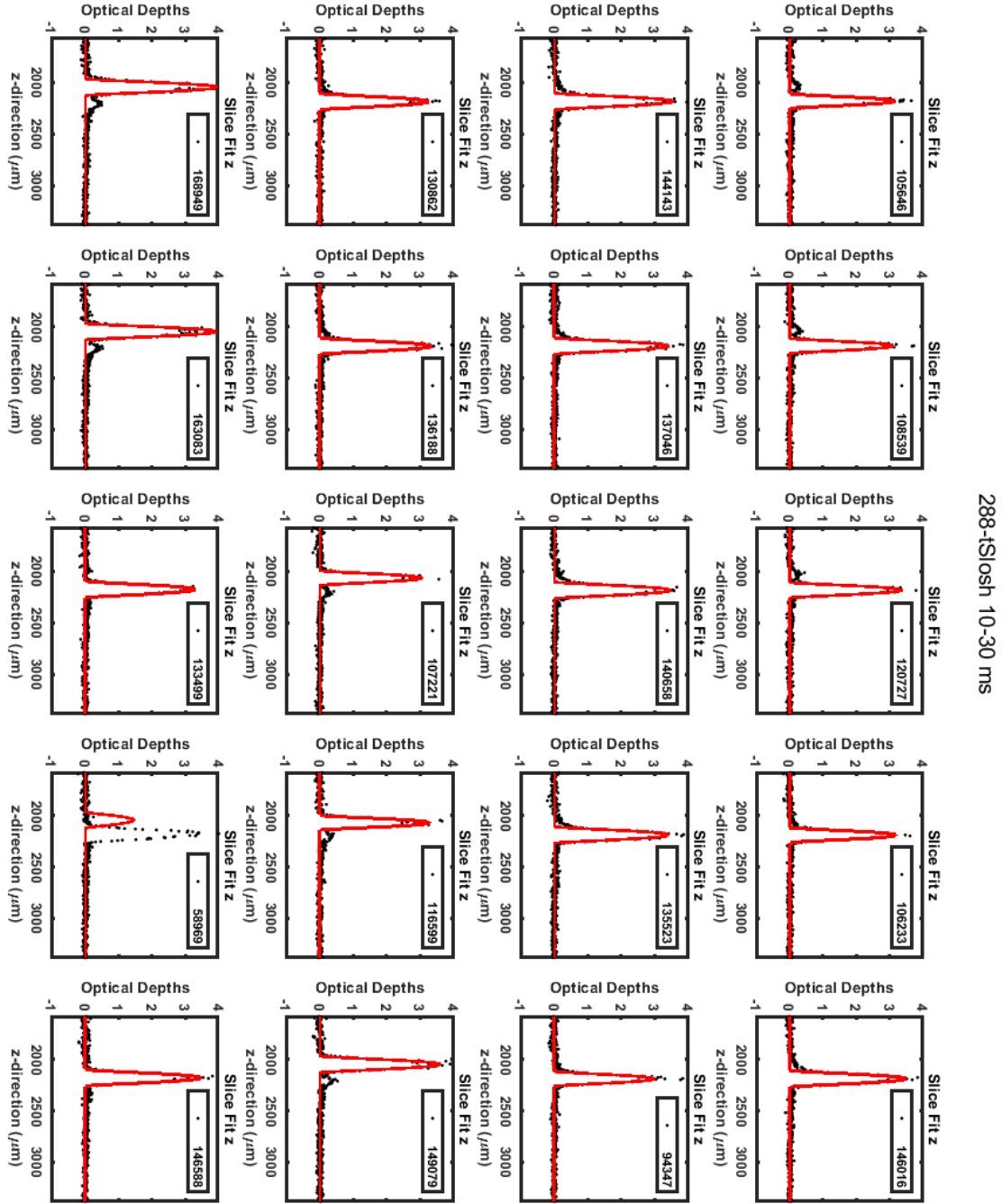


Figure 4.5: A set of slice fits with reported  $N$  from short TOF,  $t_0 = 4$  ms, trials taken in the first trap configuration.

$N = 90000$ - $170000$ . Figure 4.4 is a distribution of the atom numbers I report across these trials.

### 4.3 UFOs (Unidentified Free-falling Objects)

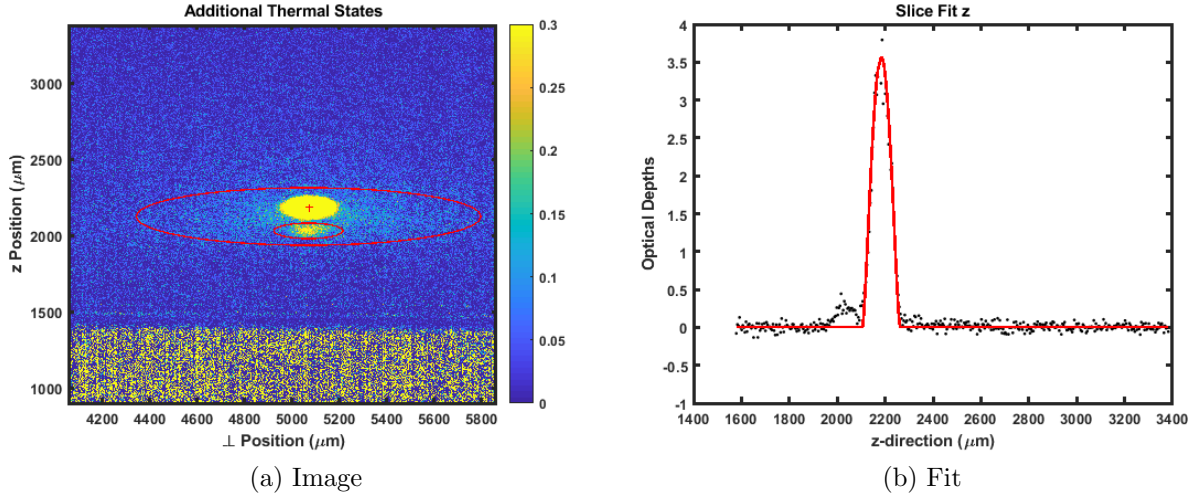


Figure 4.6: (a) Additional states discovered during a sloshing trial. The large ellipse denotes the  $|2, 0\rangle$  untrapped state. The small ellipse denotes the  $|2, 1\rangle$  weakly trapped state. The red “+” denotes a COM calculation over the whole region. Do to the more relaxed nature of the  $|2, 1\rangle$  trap, the two cloud appear out of phase. This sloshing behavior is discussed more in Section 4.4. (b) Fit about a slice through the perpendicular center, with the  $|2, 1\rangle$  state ostensibly present and out of phase.  $N \sim 150000$ . The presence of the additional state is negligible to the TF fit and our ability to determine  $N$  of the condensate.

In this section I address the presence of additional states from the evaporative cooling process we employ near the surface of the atom chip. We expect a bimodal fit to capture all of the peaks present within our optical density profile, however in some of the data presented within this thesis we note a small population of atoms experiencing a different potential from the trap confining the condensate. These additional states consist of a small thermal cloud in the  $|2, 1\rangle$  potential, and a large encompassing halo of the untrapped  $|2, 0\rangle$  atoms. Their existence in short TOF provokes consideration for whether we may need more thermal modes within our fitting function of these experiments. Luckily, the density of atoms in the condensate far exceeds that of any of these other untrapped or weakly confined states. Therefore we are able to still fit the condensate effectively by optimizing the TF mode to latch on to the peak of highest  $\mathcal{OD}$ . These additional states however become an issue in the fitting a thermal component to the

$|2, 2\rangle$  atoms, as they both have optical number densities of similar order. Conversely for long TOF we note some of these additional state to have dispersed from the frame of imaging. For now my code's ability to determine a condensate fraction is limited to the use of our predicted  $T_c$  and our estimation of  $T$ .

## 4.4 Trap Frequency Characterization via Non-Adiabatic Ramp

In ramping down the uniform strength of the CAL trap bias fields I have argued that we can translate and relax the trapping potential in space. Considering only a single dimension for a moment, these two degrees of motion both risk the possibility of exciting atoms within the condensate. Whether we choose to think about adiabaticity from its place in quantum physics or from thermodynamics, the goal is to consider how the operations we perform on our condensate effect the state composition of our cloud. In expanding the potential we increase the system's energy spacing, and if done too quickly we risk projecting the old trap's ground state onto the basis of eigenfunctions for the new trap. In translating the potential we are temporarily displacing the condensate to a point of higher potential energy in the trap. If we do not gradually return the condensate to its minimum after this translation then some of that potential energy will get converted to kinetic and the ground state fraction will decrease.

While in practice the expansion from the tight trap to the new, wider trap is generally slow enough to retain adiabaticity, in the process of translated the trap center the impulse of stopping this motion can happen on a small enough timescale to excite the system. For the rest of this section I will address one application of purposefully inducing non-adiabaticity in the ramping down of the CAL bias fields. If at the end of this ramp we instantaneously stop varying the bias field in one dimension, the potential held by the condensate is converted into a small amount of kinetic energy. Atoms for which this is not enough energy to become excited out of the ground state we can think of as classically sloshing up and down the walls of the potential. Since the potential is harmonic we expect atoms in the condensate to undergo a simple harmonic

motion the we can characterize by the ground state frequency of the condensate's center-of-mass in the trap.

By varying the amount of time after this ramp (TIT) [before turning off the potential altogether for TOF imaging] and preserving all other components of our experiment, we take images of the condensate at different points in the phase of this harmonic motion. If the sloshing behavior can effectively be preserved to 1D then by fitting the motion of the center of the condensate to a single sinusoidal curve as we vary TIT allows us to determine a value for the frequency of this oscillation. The following results are determinations of  $\omega_z$  from a 100 ms linear ramp of the  $z$  bias field. Note that this 100 ms is a very slow timescale for decompression, but the discontinuity of when we stop decreasing the bias field can excite the atoms for any decompression timescale.

At the end of Section 3.2 I presented predictions for the frequencies of two final trapping configurations within the experiment. I will now compare the results of my fit with these predictions. Confidence bounds are determined from a combination of the error in  $\omega_z$  and in  $z_0$ , both determined from maximum and minimum coefficients of each fit. For the first trapping

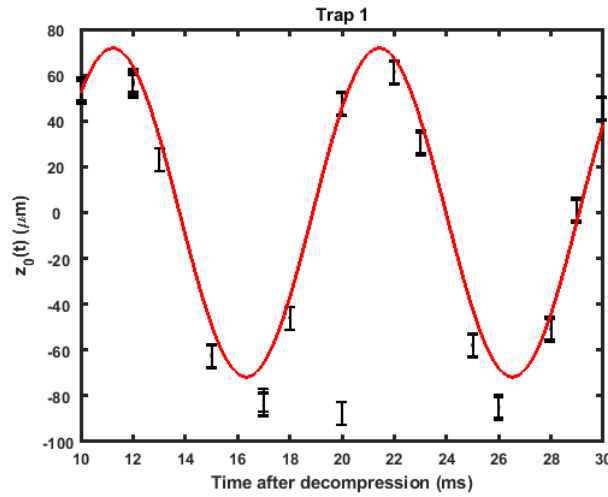


Figure 4.7: Characterization of  $z$  trap frequency for the first trap configuration. From the configuration's initial tight trap the bias fields were linear ramped down to their final value over the span of 100 ms. Each data point represents a different variable of time after the linear ramp had completed.

configurations our model predicts  $\omega_z = 2\pi \cdot 100.8$  Hz. The results of varying TIT from 10 ms to 30 ms and fitting the oscillation of  $z_0$ , yields a value  $\omega_z = 2\pi \cdot (98 \pm 4)$  Hz. This is within good reason and the error is less then 5% of the best value. Figure 4.7 depicts this fit. We can



see some general disagreement between the amplitude of the motion in the data and the fit, but this is inconsequential for the fit's ability to determine frequency.

For the second trapping configurations our model predicts  $\omega_z = 2\pi \cdot 87.1$  Hz. The results of varying TIT on the same 20 ms interval and fitting the oscillation of  $z_0$ , yields a value  $\omega_z = 2\pi \cdot (90 \pm 4)$  Hz. The error remains within 5% of the best value. Furthermore it effectively captures the predictions within these bounds. Figure 4.8 displays this fit. If anything these are pleasing results as they indicate a shared understanding between theory and experiment, let alone the exact precision of each fit.

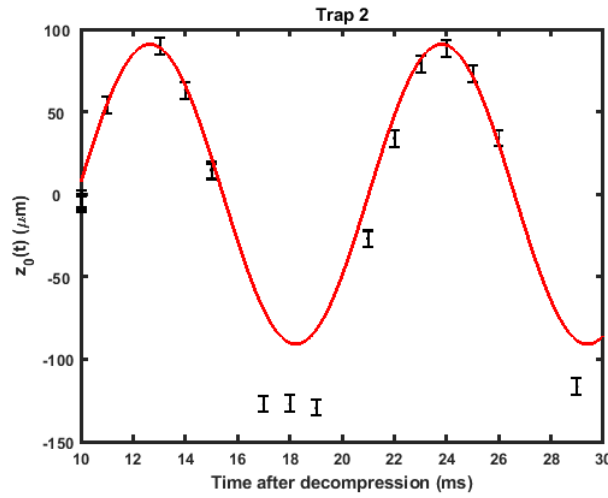


Figure 4.8: Characterization of  $z$  trap frequency for the first trap configuration. From this configuration's initial tight trap, we perform the same linear ramp and vary TIT on the same 20 ms interval.

## 4.5 Adiabatic Ramp and Mysterious Heating

In the last section we discussed the scenario of instantaneously changing the slope of our linear ramp from a negative constant to zero. This path the condensate follows excites the ground state oscillation of the condensate's center-of-mass in its confining potential. If the path by which we vary the bias fields gradually brings the condensate to rest at the minimum of the potential then this excitation does not occur. This section details the ongoing work in producing these adiabatic ramps. To make this happen, the slope of the bias field over time should gradually transition from negative to zero, rather than instantaneously turning off. In

practice we follow a 500 ms decompression that's shape resembles a hyperbolic tangent function decomposed into 20 linear steps.

We expect to observe condensates at temperatures lower than those in the trials of the last section, however we find a hot thermal cloud with virtually no condensate fraction. At temperatures in the range of 280-310 nK, these estimations are far hotter than the thermal components of the condensates fitted in long TOF. Additionally the temperatures we find from the data set are higher than the predicted  $T_c$  for the weak trap the atomic cloud experiences before imaging. This begs the question of whether the atoms have entered their thermal regime of the trap during the process of this ramp. The root of this mysterious heating is entirely open-ended, however I present some discussion of possible sources in Section 5.1.

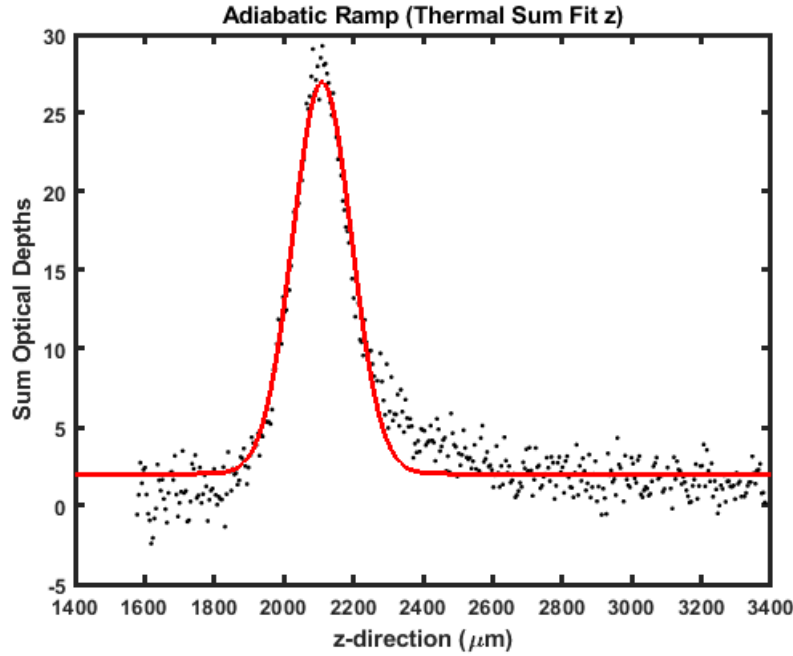


Figure 4.9: Thermal cloud after 500 ms tanh decompression into first trap configuration.  $T = 290$  nK, leading to no expected condensate fraction.

# Chapter 5

## Looking Forward

In this chapter I discuss the random heating effect we observe in Section 4.5 in adiabatically ramping the bias magnetic fields down to their final levels. A significant distinguishing feature of this ramp is the 400 ms of additional time that our condensate spends in a tighter confinement, with strong magnetic fields still on. I strongly reiterate the open-ended nature of the questions surrounding this observed heating, posed by this thesis, and the potential sources referenced are merely food for thought.

Lastly I will return once again to my tools of analysis. There are number of ways in which this code can be further improved upon and I discuss a next step that can be taken. Additionally I discuss some of the error in my calculations of atom number and temperature.

### 5.1 Mysterious Heating

There are two categories for which we consider sources of this heating effect: 1.) a short timescale time-dependent potential the atoms experience, and 2.) random inelastic collisions that occur in our species of atom in tight confinement. Both of these concerns scale with the time that the CAL apparatus is actively engaging a tight magnetic confinement. The information presented here represents a brief review of our current understanding of these two categories.

The former set of concerns we present very generally describes a situation in which our trapping potential varies with time on a non-adiabatic timescale for the atoms in the trap. A significant amount of background noise in the magnetic field could effectively induce a perturbation upon atoms in the trap. Near the surface of the atom chip, research demonstrates the possibility of that level of noise[51, 52]. In our experiment the gradual tanh approximation we make in this ramp means that the atoms spend more time near the surface of the chip than in other experiments presented within this thesis.

Another potential source of this heating could be entirely independent from the noise of our apparatus. For  $^{87}\text{Rb}$  there are two distinct forms of inelastic collision that naturally can occur when we bring the atoms in tight enough confinement. The first of these collision are between three atoms in which two combine to form a small molecule and the other is sent off with the kinetic energy of the collision. This process heats up the condensate as the energy of this collision is typically much larger than the potential wells we study here[53, 54]. The other form of inelastic collisions predicted for Rb happens between two atoms in which there occurs a  $\Delta m_F$  transition as a result of the collision[55]. This would stimulate loss from the trap at points where atoms are more dense for reasons discussed primarily in Section 2.4. While this too presents a source of potential heating, the rate at which it is predicted to occur is negligible[56]. However the longer our condensate spends in tight confinement the more the conditions for these collisions are made available.

## 5.2 Returning the to Fits

I will now extrapolate a little further upon my analysis. In Section 4.3 I discussed the existence of additional states present in our system in short TOF. In these images we note the presence of the  $|2, 1\rangle$  state as a small blip of  $0.1 < \mathcal{OD} < 0.5$ , out of phase with the condensate. The  $|2, 0\rangle$  states are more difficult to determine the presence of as we expect them to have the distribution of a large wide Gaussian with minimal  $\mathcal{OD} \leq 0.1$ . This of a similar order to the background noise threshold we experience and could be doing some work to mask the full height of the  $\mathcal{OD}$  distribution. Furthermore the expansion dynamics we discussed for thermal clouds

in Section 2.5 are described to be the weakest for this dilute gas experiencing no potential in space, meaning that these atoms can potentially hang around for longer TOF. One solution to this problem is to shrink the excised fitting region to contain a small enough portion of the wide thermal  $|2, 0\rangle$  distribution such that we can approximate it to be flat within the frame. We can then concatenate the information from this optical density distribution into the noise floor  $N$  that we measure with our fit.

While this allows us to more smoothly apply a bimodal thermal + TF fit, the information about the widths of each distribution inevitable gets lost, into this new noise floor. The width of the Thomas-Fermi distribution varies on a much smaller degree near the base of the distribution than for our description of a thermal cloud. This limits our ability to effectively calculate a temperature for the relatively small thermal components of the condensates we image. The propagation of uncertainty for polynomials for Equation (4.8) tells that that if there is a 5% error in the fit's estimation of  $\sigma_i$  then  $T$  could have an error on the order of twice that, 10%.

I also would like to return briefly to the difficulties I discussed in capturing a measure of peak optical density. While saturation of optical depths affects our ability to capture the true peak of the cloud, this artificial noise floor also serves as a limiter on our fits calculations of a peak optical density  $n_0$ , and subsequently on our calculation of atom number  $N$ .

That being said, I was able to demonstrate the accuracy with which we can measure the center-of-mass of these distributions under any conditions. Our confidence of this center is to within  $< 5\%$  of the width of the distribution, indicating that we are relatively certain of a center existing within the walls of the distribution. This information is central to further experimentation with CAL, as we need to have an exact spatial map of where our magnetic fields are in order to produce the kind of adiabatic potential we hope to explore soon.

# References

- [1] H       Perrin and Barry M. Garraway. Trapping atoms with radio frequency adiabatic potentials. In *Advances In Atomic, Molecular, and Optical Physics*, pages 181–262. Elsevier, 2017.
- [2] O. Zobay and B. M. Garraway. Atom trapping and two-dimensional bose-einstein condensates in field-induced adiabatic potentials. *Physical Review A*, 69(2), February 2004.
- [3] Nathan Lundblad, Thomas Jarvis, Daniel Paseltiner, and Courtney Lannert, 2016. <http://meetings.aps.org/link/BAPS.2016.DAMOP.K1.119>.
- [4] Daniel Adkins Paseltiner. Progress towards bose-einstein condensation on an atom chip as a functional testbed for experiments aboard the orbital NASA Cold Atom Laboratory. 2016.
- [5] Kuei Sun, Karmela Padavi  , Frances Yang, Smitha Vishveshwara, and Courtney Lannert. Static and dynamic properties of shell-shaped condensates. *Physical Review A*, 98(1), July 2018.
- [6] Romain Dubessy, Camilla De Rossi, Mathieu de Gor De Herve, Thomas Badr, Aur       Perrin, Laurent Longchambon, and H       Perrin. Local correlations reveal the superfluid to normal boundary in a trapped two-dimensional quantum gas. 2018.
- [7] Z Hadzibabic, P Kr      , M Cheneau, S P Rath, and J Dalibard. The trapped two-dimensional bose gas: from bose–einstein condensation to berezinskii–kosterlitz–thouless physics. *New Journal of Physics*, 10(4):045006, April 2008.

- [8] O. Zobay and B. M. Garraway. Two-dimensional atom trapping in field-induced adiabatic potentials. *Physical Review Letters*, 86(7):1195–1198, February 2001.
- [9] Drop tower website. <https://www.zarm.uni-bremen.de/en/drop-tower/general-information.html>.
- [10] T. van Zoest. Bose-einstein condensation in microgravity. *Science*, 328(5985):1540–1543, June 2010.
- [11] Sascha Kulas. Miniaturized lab system for future cold atom experiments in microgravity. *Microgravity Science and Technology*, 29(1-2):37–48, November 2016.
- [12] MAIUS-1. [https://www.dlr.de/dlr/en/desktopdefault.aspx/tabid-10081/151\\_read-20337/gallery/25194/gallery/25194](https://www.dlr.de/dlr/en/desktopdefault.aspx/tabid-10081/151_read-20337/gallery/25194/gallery/25194).
- [13] Matthias Lezius. Space-borne frequency comb metrology. *Optica*, 3(12):1381, November 2016.
- [14] Elizabeth Gibney. Universe’s coolest lab set to open up quantum world. *Nature*, 557(7704):151–152, May 2018.
- [15] Ethan R. Elliott, Markus C. Krutzik, Jason R. Williams, Robert J. Thompson, and David C. Aveline. NASA’s cold atom lab (CAL): system development and ground test status. *npj Microgravity*, 4(1), August 2018.
- [16] Nathan Lundblad, Ryan Carollo, and Xiaole Jiang. Model.
- [17] Daniel V Schroeder. An introduction to thermal physics, 1999.
- [18] CJ Foot. *Atomic physics*. Oxford University Press, USA, 2005.
- [19] C. Pethick and H. Smith. *Bose-Einstein condensation in dilute gases*. Cambridge University Press, 2002.
- [20] Harold J. Metcalf and Peter van der Straten. *Laser Cooling and Trapping*. Springer-Verlag, New York, 1999.

- [21] David J. Griffiths. *Introduction to Quantum Mechanics (2nd Edition)*. Pearson Prentice Hall, 2nd edition, April 2004.
- [22] S Giorgini, LP Pitaevskii, and S Stringari. Condensate fraction and critical temperature of a trapped interacting bose gas. *Physical Review A*, 54(6):R4633, 1996.
- [23] L. H. Thomas. The calculation of atomic fields. *Mathematical Proceedings of the Cambridge Philosophical Society*, 23(05):542, January 1927.
- [24] Silvan S. Schweber. Enrico fermi and quantum electrodynamics, 1929–32. *Physics Today*, 55(6):31–36, June 2002.
- [25] Max Born. *The restless universe*, volume 412. Courier Corporation, 1951.
- [26] David Chen. Atomic gas density profile, November 2012.
- [27] M. Egorov, B. Opanchuk, P. Drummond, B. V. Hall, P. Hannaford, and A. I. Sidorov. Measurement of s-wave scattering lengths in a two-component bose-einstein condensate. *Physical Review A*, 87(5), May 2013.
- [28] D. M. Harber, H. J. Lewandowski, J. M. McGuirk, and E. A. Cornell. Effect of cold collisions on spin coherence and resonance shifts in a magnetically trapped ultracold gas. *Physical Review A*, 66(5), November 2002.
- [29] R. Côté, A. Dalgarno, H. Wang, and W. C. Stwalley. Potassium scattering lengths and prospects for bose-einstein condensation and sympathetic cooling. *Physical Review A*, 57(6):R4118–R4121, June 1998.
- [30] Daniel A. Steck. Rubidium 87 d line data, October 2003.
- [31] Nathan Lundblad. Personal correspondence, June 2018. Yes you can still find them on amazon: <https://www.amazon.com/Puuli-Optical-X-4908-203-1-Lasereinheit-X49082031/dp/B018E42LX2>.
- [32] Carlos L. Garrido Alzar, Hélène Perrin, Barry M. Garraway, and Vincent Lorent. Evaporative cooling in a radio-frequency trap. *Physical Review A*, 74(5), November 2006.



- [33] William D. Phillips. Nobel lecture: Laser cooling and trapping of neutral atoms. *Reviews of Modern Physics*, 70(3):721–741, July 1998.
- [34] D. J. Wineland, R. E. Drullinger, and F. L. Walls. Radiation-pressure cooling of bound resonant absorbers. *Physical Review Letters*, 40(25):1639–1642, June 1978.
- [35] Walther Gerlach and Otto Stern. Der experimentelle nachweis der richtungsquantelung im magnetfeld. *Zeitschrift fr Physik*, 9(1):349–352, December 1922.
- [36] Philippe Bouyer, Vincent Boyer, SG Murdoch, Guillaume Delannoy, Yann Le Coq, Alain Aspect, and Michel L  crivain. Rf-induced evaporative cooling and BEC in a high magnetic field. In *Bose-Einstein Condensates and Atom Lasers*, pages 165–186. Springer, 2002.
- [37] Y. Castin and R. Dum. Bose-einstein condensates in time dependent traps. *Physical Review Letters*, 77(27):5315–5319, December 1996.
- [38] EXpedite the PROcessing of Experiments to Space Station Rack (EXPRESS Rack). [https://www.nasa.gov/mission\\_pages/station/research/experiments/608.html](https://www.nasa.gov/mission_pages/station/research/experiments/608.html).
- [39] Cold Atom Laboratory. <https://coldatomlab.jpl.nasa.gov/>.
- [40] ColdQuanta. <https://www.coldquanta.com/>.
- [41] Wolfgang H  nsel, Peter Hommelhoff, TW H  nsch, and Jakob Reichel. Bose–einstein condensation on a microelectronic chip. *Nature*, 413(6855):498, 2001.
- [42] A. E. Leanhardt, Y. Shin, A. P. Chikkatur, D. Kielpinski, W. Ketterle, and D. E. Pritchard. Bose-einstein condensates near a microfabricated surface. *Physical Review Letters*, 90(10), March 2003.
- [43] Daniel M Farkas, Evan A Salim, and Jaime Ramirez-Serrano. Production of rubidium bose-einstein condensates at a 1 hz rate. *arXiv preprint arXiv:1403.4641*, 2014.
- [44] M. Trinker, S. Groth, S. Haslinger, S. Manz, T. Betz, S. Schneider, I. Bar-Joseph, T. Schumm, and J. Schmiedmayer. Multilayer atom chips for versatile atom micromanipulation. *Applied Physics Letters*, 92(25):254102, June 2008.

- [45] Rob Thompson and Anita Sengupta. Cold Atom Laboratory “The Coolest Spot in the Universe”, June 2017. Poster presented online at CAL website.
- [46] Daniel M. Farkas, Kai M. Hudek, Shengwang Du, and Dana Z. Anderson. Efficient direct evaporative cooling in an atom-chip magnetic trap. *Physical Review A*, 87(5), May 2013.
- [47] Y Colombe, E Knyazchyan, O Morizot, B Mercier, V Lorent, and H Perrin. Ultracold atoms confined in rf-induced two-dimensional trapping potentials. *Europhysics Letters (EPL)*, 67(4):593–599, August 2004.
- [48] K Merloti, R Dubessy, L Longchambon, A Perrin, P-E Pottie, V Lorent, and H Perrin. A two-dimensional quantum gas in a magnetic trap. *New Journal of Physics*, 15(3):033007, March 2013.
- [49] Nathan Lundblad. Personal correspondence.
- [50] Heather J Lewandowski, DM Harber, Dwight L Whitaker, and Eric A Cornell. Simplified system for creating a bose–einstein condensate. *Journal of low temperature physics*, 132(5-6):309–367, 2003.
- [51] Mark Keil, Omer Amit, Shuyu Zhou, David Groswasser, Yonathan Japha, and Ron Folman. Fifteen years of cold matter on the atom chip: promise, realizations, and prospects. *Journal of Modern Optics*, 63(18):1840–1885, May 2016.
- [52] P. Krüger, L. M. Andersson, S. Wildermuth, S. Hofferberth, E. Haller, S. Aigner, S. Groth, I. Bar-Joseph, and J. Schmiedmayer. Potential roughness near lithographically fabricated atom chips. *Physical Review A*, 76(6), December 2007.
- [53] J. Söding, D. Guéry-Odelin, P. Desbiolles, F. Chevy, H. Inamori, and J. Dalibard. Three-body decay of a rubidium bose–einstein condensate. *Applied Physics B*, 69(4):257–261, October 1999.
- [54] JP DIncao, J Von Stecher, and Chris H Greene. Universal four-boson states in ultracold molecular gases: Resonant effects in dimer-dimer collisions. *Physical review letters*, 103(3):033004, 2009.

- [55] A Sartori, J Marino, S Stringari, and A Recati. Spin-dipole oscillation and relaxation of coherently coupled bose–einstein condensates. *New Journal of Physics*, 17(9):093036, September 2015.
- [56] P. S. Julienne, F. H. Mies, E. Tiesinga, and C. J. Williams. Collisional stability of double bose condensates. *Physical Review Letters*, 78(10):1880–1883, March 1997.